The use of imaging flow cytometry for rapid, high-throughput and automated analysis of the *Leishmania mexicana* promastigote cell cycle provides new insights into cell cycle events of short duration.

Short title: Imaging flow cytometry analysis of the *L. mexicana* cell cycle

Jessie Howell[1], Sulochana Omwenga[2], Melanie Jimenez[3] and Tansy C. Hammarton[2]*

[1]James Watt School of Engineering, University of Glasgow, Glasgow, United Kingdom

[2]School of Infection and Immunity, University of Glasgow, Glasgow, United Kingdom

[3]Biomedical Engineering Department, University of Strathclyde, Glasgow, United Kingdom

[*]Corresponding author. Email: Tansy.Hammarton@glasgow.ac.uk (TH)

Abstract

Promastigote *Leishmania mexicana* have a complex cell division cycle characterised by the ordered replication of several single-copy organelles, a prolonged S phase and very rapid G2 and cytokinesis phases, accompanied by cell cycle stage-associated morphological changes. Here we exploit these morphological changes to develop a high-throughput and semi-automated imaging flow cytometry (IFC) pipeline to analyse the cell cycle of *L. mexicana* in live cells. Firstly, we demonstrate that, unlike several other DNA stains, Vybrant™ DyeCycle™ Orange (DCO) is non-toxic and enables quantitative DNA imaging in live *L. mexicana* promastigotes. Secondly, by tagging the orphan spindle kinesin, KINF, with mNeonGreen, we describe KINF's cell cycle-dependent expression and localisation. Then, by combining manual gating of DCO DNA intensity profiles with automated masking and morphological measurements of parasite images, visual determination of the number of flagella per cell, and automated masking and analysis of mNG:KINF fluorescence, we provide a newly detailed description of *L. mexicana* promastigote cell cycle events that, for the first time, includes the durations of individual G2, mitosis and post-mitosis phases. By applying IFC in this way, we were able, in minutes, to capture tens of thousands of high-quality brightfield and fluorescent images of live *L. mexicana* cells in solution, and to acquire quantitative data across multiple parameters for every image captured. Our custom-developed masking and gating scheme allowed us to identify elusive G2 cells, show that cytokinesis commences during early mitosis and continues after mitosis is complete, and identify newly divided cells that were within the first 12 minutes of the new cell cycle. Our new pipeline offers many advantages over traditional methods of cell cycle analysis such as fluorescence microscopy and flow cytometry and paves the way for novel high-throughput analysis of *Leishmania* cell division.

Author Summary

Leishmania mexicana is a single-celled parasite that is spread by sand flies and causes a spectrum of diseases called the leishmaniases in humans and animals. To cause disease, *L. mexicana* parasites must replicate and divide, and their cell division cycle has unusual and complex features, including that the parasite changes shape as it replicates. To aid analysis of the *L. mexicana* cell cycle, we developed a new quantitative DNA staining technique and also generated a fluorescent parasite cell line that highlighted when cells were dividing their DNA after replicating it (mitosis). We then applied a high-throughput technique called imaging flow cytometry to capture images of tens of thousands of these parasites in just a few minutes. For each image, we were able to extract data about DNA replication, cell shape and also whether the cells were in mitosis or not. This provided new insights into how the parasites divide and how long each stage of cell division takes. More importantly, the imaging pipelines we have developed offer great advantages in terms of speed and depth over more traditional analysis techniques such as microscopy and should pave the way for increasingly detailed analyses of parasite cell biology in the future.

58 **Introduction**

59 *Leishmania* spp. are unicellular parasitic protists responsible for the leishmaniases, a
60 heterogenous group of neglected tropical diseases that affect humans and animals, causing
61 disfiguring and potentially disabling cutaneous lesions to fatal visceral disease. Over 20
62 species of *Leishmania* can cause disease in humans, and there are more than 90 sand fly
63 vector species that transmit the parasites between hosts (https://www.who.int/news-
64 room/fact-sheets/detail/leishmaniasis). Key to being able to complete its digenetic life cycle
65 and to cause disease in humans and animals, is the ability of the parasite to proliferate in its
66 hosts. Thus, understanding better how its cell cycle is regulated at the molecular level could
67 offer new avenues for the development of novel therapeutics for leishmaniasis.

68 *Leishmania* are members of the Kinetoplastida, an order characterised by the presence of
69 two DNA-containing organelles: the nucleus, and the kinetoplast, which contains the genome
70 of the organism's single mitochondrion. The kinetoplast is linked to a pair of basal bodies
71 comprising one immature pro-basal body and one mature basal body that subtends a single
72 flagellum. The flagellum emerges from the cell body via a specialized invagination of the
73 plasma membrane termed the flagellar pocket, which likely acts as the sole site of endo- and
74 exocytosis in the cell (1). *Leishmania* also possess a single Golgi apparatus, located
75 between the nucleus and kinetoplast, and beneath the plasma membrane is a subpellicular
76 microtubule cytoskeleton that remains assembled throughout the cell cycle. Replication and
77 segregation of the single copy organelles occurs in a precise order to ensure that two viable
78 daughter cells are generated post-cell division, and, in procyclic promastigote parasites,
79 these events are accompanied by significant changes in cell morphology (1, 2) (S1 Fig).

80 At the start of the cell cycle (G1 phase), *Leishmania* promastigotes possess one nucleus (N),
81 one kinetoplast (K) and one flagellum (F) (S1 Fig). During G1, the cell body doubles in
82 length, but not in width (2). The cell length then remains constant while DNA is replicated
83 during S phase. About one hour before the end of S phase, basal body maturation occurs to
84 nucleate the growth of a new flagellar axoneme, but the second flagellum only becomes

visible by light microscopy when it emerges from the flagellar pocket around the end of S phase. Within the post-S phase period, G2 phase has not been precisely defined for *Leishmania*, and is assumed to be very brief (2). Mitosis then ensues – in *L. mexicana*, the nucleus divides before the kinetoplast (2), although the order is reversed in other *Leishmania* species (3, 4). G2 and mitosis are accompanied by a reduction in cell length and a simultaneous expansion in cell width. Finally, cytokinesis, which involves localised remodelling of the microtubule cytoskeleton and invagination of the plasma membrane to form a cleavage furrow to bisect the cell, completes the cell cycle (2, 4).

Thus, cell morphology and organelle replication are intricately linked in *Leishmania* procyclic promastigotes. Parasite cell cycle progression is commonly assessed through visualization of organelles (through staining, immunofluorescence or the use of fluorescent marker proteins) alongside observation of cell morphology, as well as quantitation of DNA content *via* flow cytometry (typically using fixed cells stained with propidium iodide) (2, 5-7). These methods are not without their limitations, though. While microscopy can provide high resolution spatial information, it can be highly labour-intensive if performed manually, especially if rare populations of cells are being studied, large numbers of cells are required for the analysis or measurements of cell morphology (e.g. length, width) are performed by hand using software such as ImageJ/Fiji (2, 8). Further, artefacts can be introduced if live cells are imaged for extended periods without the use of an environmental chamber, or if cells are fixed prior to staining. Conversely, flow cytometry approaches are high-throughput and can provide information on total DNA (or protein) content within a cell, but they do not offer information on how the DNA is packaged or the localisation of proteins or structures within the cell, and only provide limited information on cell size and morphology (e.g. from side scatter measurements).

Imaging flow cytometry (IFC) (9, 10) potentially offers a powerful alternative for cell cycle analysis, since it combines the high-throughput and quantitative analysis of flow cytometry with the visual and spatial information of microscopy by capturing images in brightfield,

112 darkfield and fluorescence modes for every cell analysed. Further, the application of masks to
113 identify areas of interest allows many morphological parameters, including length, width,
114 perimeter, area, aspect ratio (AR) and circularity to be measured or calculated automatically.
115 Upon identifying the morphological properties of a population of cells of interest (for example,
116 short, wide, fluorescence positive or long, narrow, fluorescence negative), the application of
117 masks and development of a gating strategy enables the automatic classification of cells
118 matching these parameters. This has enabled the detection and morphological analysis of a
119 wide range of cell types, from phytoplankton (11, 12) to blood cells (13-15), circulating
120 endothelial and tumour cells (16-18), intracellular pathogens (19, 20) and bacteria (21).
121 Further, IFC has been used to aid or automate cell cycle analysis of human cell lines and
122 fission yeast, both with stained cell populations (22-24) and in unlabelled cells (25), and can
123 also increase the throughput and reproducibility of assays that detect subcellular phenotypes
124 and activities, for example, DNA damage (26, 27), multinuclearity (28), changes to organelle
125 structure or morphology (29, 30) and nucleocytoplasmic shuttling of proteins (31). While IFC
126 has previously been used to analyse several aspects of kinetoplastid biology (32-34), it has
127 not, to our knowledge, been used to study their cell cycle.

128 Here we aimed to investigate if IFC could be applied to study the *Leishmania* cell cycle and
129 whether it offered advantages over conventional methods of cell cycle analysis. We
130 demonstrate that IFC offers a high throughput and convenient approach for analysing the
131 *Leishmania* cell cycle in live cells. We find that Vybrant™ DyeCycle™ Orange quantitatively
132 stains DNA in live promastigote cells and when combined with automated IFC measurements
133 of cell body length and width, allows discrimination between early and late G1 phase cells, S
134 phase, and G2/M/cytokinesis cells. Further, by tagging the orphan kinesin, KINF, with
135 mNeonGreen, we use IFC to detail its cell cycle-dependent expression and localisation, and
136 use the tagged cell line to provide greater resolution of cell cycle stages. For the first time, this
137 allowed G2 cells to be distinguished from cells undergoing mitosis or cytokinesis, the durations
138 of G2 and the post-mitotic period to be quantified, and newly divided G1 cells to be identified.

139 The ability to capture tens of thousands of cell images within a few minutes, measure multiple
140 morphological and fluorescence parameters for every cell, and then apply custom gates to
141 automatically identify populations of interest, provides a step-change in the type and scale of
142 analysis of *Leishmania*'s cell cycle and cell biology. Significantly, when applied to live cells,
143 IFC offers near real-time analysis of perturbations within a population.

144

145 # Results

146 **Imaging flow cytometry is suitable for morphological analysis of *L. mexicana***

147 To determine whether IFC is a suitable tool to analyse the *L. mexicana* promastigote cell
148 cycle, live and paraformaldehyde (PFA)- or methanol-fixed parasites were analysed by IFC
149 to confirm that the previously reported cell cycle-dependent changes in cell morphology (2)
150 could be observed (Fig 1). Cells with morphologies corresponding to all cell cycle stages
151 were observed in the live and fixed populations, although some methanol-fixed cells
152 appeared to have aberrant morphology (with cells appearing fatter and more rounded) (Fig
153 1A). Measurements of length and width calculated using a cell body mask (Fig 1B,C)
154 revealed that both PFA- and methanol-fixed cells were shorter in length (on average by
155 around 8.8% and 38.1%, respectively) and wider (7.2% and 8.1%) than live cells (Fig 1D),
156 indicating that fixing cells in solution alters their morphological parameters. For this study,
157 therefore, only live cells were imaged.

158

159

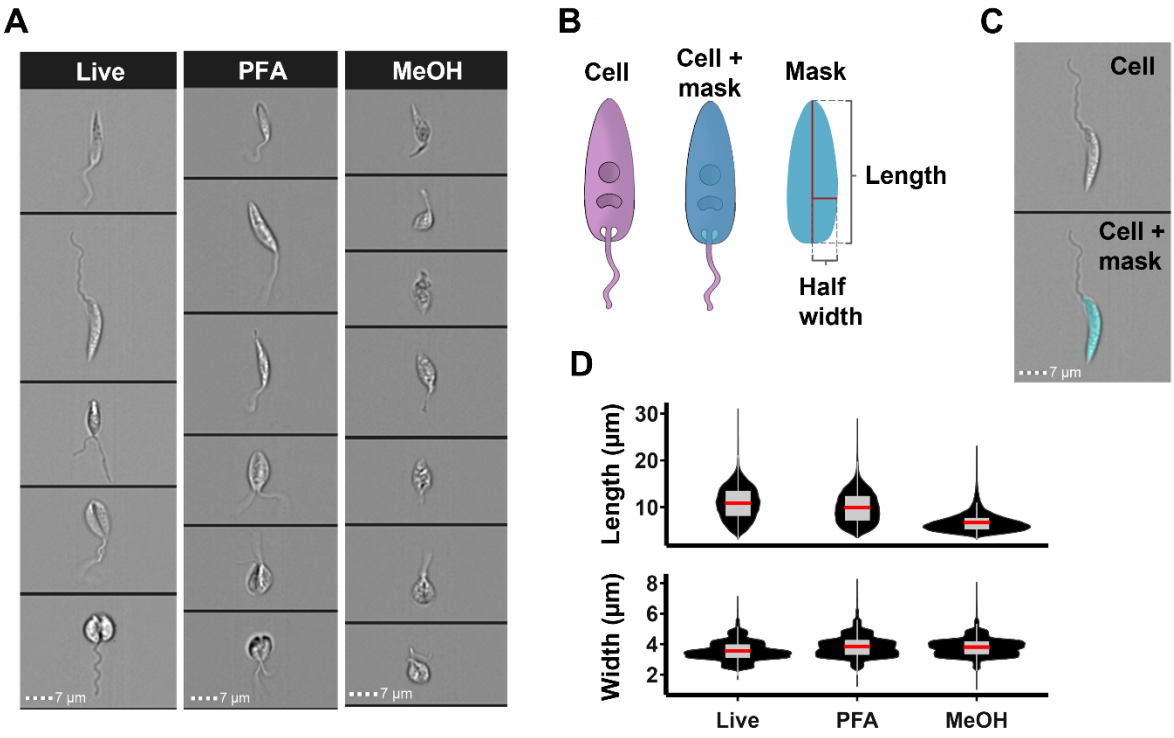

160

161 **Fig 1. Analysis of *L. mexicana* promastigote morphology using IFC.**

162 (A) IFC images from live and PFA- or methanol (MeOH)-fixed promastigote *L. mexicana* C9T7 cells.

163 (B) Schematic of cell body mask-based morphological measurements used for IFC analysis. (C)

164 Images of a cell with and without a mask. (D) Violin plots of the length and width of cell populations

165 from masked IFC images (*n* >26,499). The box plots show the 25th and the 75th percentiles, and the

166 mean in red. The whiskers represent the median +/- 1.5X interquartile range. Scale bars (dotted

167 lines): 7 µm. See S1A Table for raw data.

168

169

170

171 **Vybrant™ DyeCycle™ Orange quantitatively stains DNA in live *L. mexicana***
172 **promastigotes**

173 To determine the cell cycle position of individual *L. mexicana* parasites, a quantitative DNA
174 stain suitable for use in live promastigote cells was required. Propidium iodide (PI)
175 quantitatively stains DNA (S2A,B Fig), but requires cell fixation, and is thus unsuitable for
176 use in live cells. Hoechst 33342 is commonly used to stain the nucleus and kinetoplast in live
177 *Leishmania* (35-37), but IFC indicated that it does not bind proportionally to DNA (S2C Fig).
178 Images of Hoechst-stained cells revealed staining outside of the nucleus that may account
179 for it being non-quantitative (S2C Fig). DRAQ5 stained only the nucleus in the majority of
180 cells, while Vybrant™ DyeCycle™ Violet (DCV) stained both the nucleus and kinetoplast, but
181 neither were quantitative (S2D,E Fig). Vybrant™ DyeCycle™ Ruby (DCR) was also non-
182 quantitative, with staining appeared in foci throughout the cell body (S2F Fig). However,
183 Vybrant™ DyeCycle™ Orange (DCO) was found to stain both the nucleus and kinetoplast
184 throughout the cell cycle (Fig 2A), and to stain DNA quantitatively (Fig 2B,C), analogous to
185 PI in fixed cells (S2A,B Fig, Fig 2D). Incubation with DCO did not affect cell viability (S3 Fig),
186 but a marked reduction in the fluorescence of G2/M cells was observed if there was a delay
187 of >20 minutes in them being analysed by IFC following staining (S4 Fig). Hence, cells were
188 analysed by IFC immediately after incubation with DCO.
189

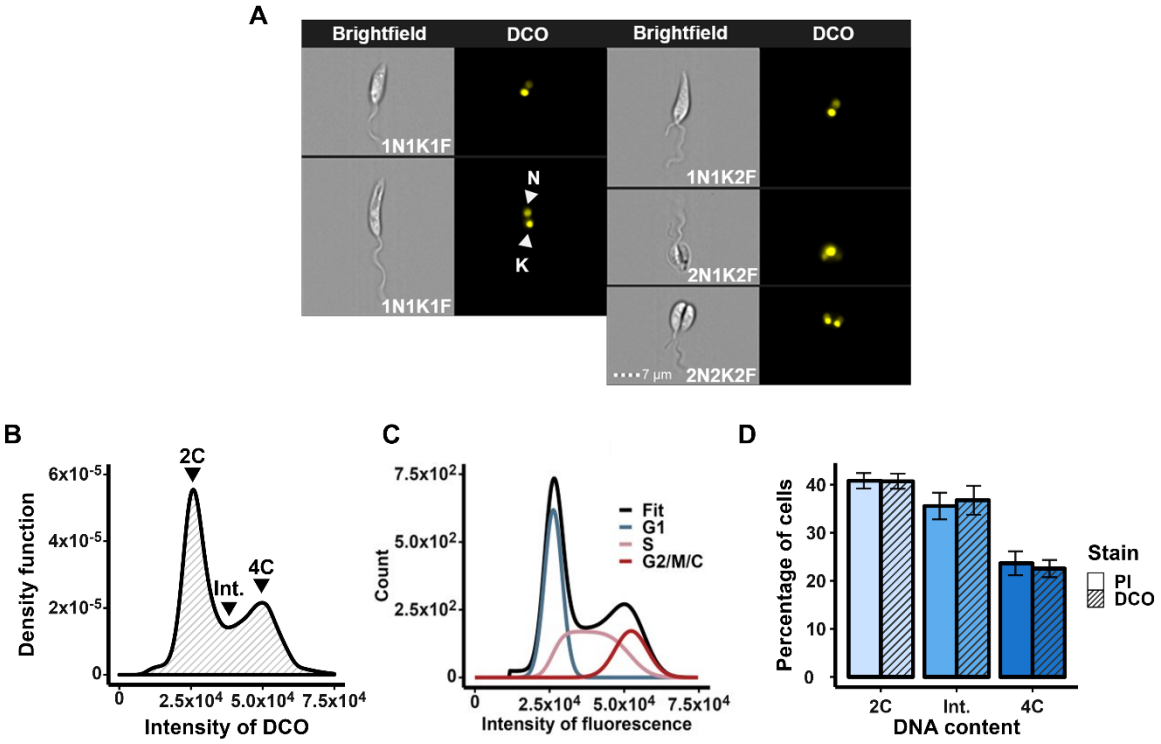

190

191 **Fig 2. DCO stains DNA quantitatively in live *L. mexicana* promastigotes**

192 (A) Brightfield and fluorescence images of *L. mexicana* promastigote C9T7 cells at different cell cycle
193 stages stained with DCO. N: nucleus; K: kinetoplast; F: flagellum. Scale bars: 7 µm. (B) The
194 fluorescence intensity profile of cells (*n* =13920) stained with DCO and analysed with IFC. Peaks are
195 indicated with arrowheads for non-replicated DNA (2C; corresponding to cells in G1 phase),
196 replicated DNA (4C; cells in G2/M phase or cytokinesis) and cells with intermediate DNA content
197 (Int.; cells undergoing S phase). (C) Cell cycle modelling of the DCO DNA intensity profile (panel B)
198 using the FCS Express™ Multicycle engine (Rabinovitch & Bagwell debris subtraction (38, 39) and
199 Dean/Jett/Fox cell cycle modelling (40)). The cell cycle stage of each curve is indicated. (D) Graph
200 comparing the proportions of cells with different DNA contents, as modelled following staining with
201 PI (S2A,B Fig) and DCO (panels B and C). Error bars represent the standard deviations of the means
202 of three replicates. See S1B Table for raw data.

203

204

205 **Automatic cell cycle classification of promastigote cells**

206 Due to biological variation and the cell cycle being a continuum, there is an overlap in the
207 DNA contents of cells in G1 and early S phase, and of cells in late S and G2/M phases. To
208 account for this natural overlap, cell cycle mathematical models such as the Dean/Jett/Fox
209 model (40) (Fig 2C, S2B Fig) or the Watson Pragmatic curve (41) can be used to extrapolate
210 the proportions of cells in each cell cycle stage from DNA fluorescence measurements
211 obtained by flow cytometry. Alternatively, manual gating can be performed where the user
212 draws custom boundaries around the different DNA content peaks obtained (6, 42, 43). Yet
213 neither method considers the biology of the system nor can accurately classify the cell cycle
214 stage of individual cells. Indeed, it has been previously reported that due to the long S
215 phase, short G2 phase and rapid cytokinesis in *L. mexicana*, there is significant overlap of
216 cell cycle stages within DNA intensity plots (44). Given the significant morphological
217 changes of *L. mexicana* cells during the cell cycle, and the ability of IFC to link morphological
218 and DNA fluorescence data for individual cells, we hypothesised that IFC could result in
219 greater resolution in classifying the cell cycle stage of individual cells than can be obtained
220 using other methods such as microscopy and flow cytometry.

221

222 Live *L. mexicana* promastigotes were stained with DCO and fluorescence intensity profiles
223 were obtained using IFC. The 2C (G1 cells plus overlapping early S phase cells),
224 intermediate (S phase cells plus overlapping G1 and early G2 phase cells) and 4C (cells in
225 G2/M and cytokinesis, plus overlapping late S phase cells) DNA peaks were then manually
226 gated (Fig 3A). Given the ability of IFC to analyse many cellular parameters, we asked
227 which, if any, morphological parameter(s) could allow cells in different cell cycle stages to be
228 distinguished. Thirteen parameters (area, aspect ratio, brightfield intensity, circularity,
229 compactness, diameter, elongatedness, height, length, perimeter, shape ratio,
230 thickness_min and width) were plotted for cells present in each of the gates (Fig 3B, S5 Fig,
231 S6A Fig). Of these, only elongatedness, height, length, perimeter and, to some extent, width
232 offered discrimination between the cells within the three gates. Since the profiles for

233 elongatedness, height, length and perimeter were very similar, we chose to proceed with cell
234 body length, as this would allow the easiest comparison with previous morphological studies.
235 Within the 2C gate, cell body lengths displayed a broad distribution, as expected, given that
236 cells grow from their smallest length at the start of early G1, to their longest at the end of G1
237 phase, with the peak centred on 10 μm (S6A Fig). Within the intermediate (2C-4C) gate, the
238 length distribution was shifted to the right, as expected for cells in S phase, peaking at ~13.5
239 μm, although there was a shoulder of shorter cells (~18% cells with cell bodies ≤10 μm in
240 length), suggesting some overlap between G1 and S phases within this gate (S6A Fig). The
241 width distributions for each of these gates were similar (S6B Fig), with the majority of cells <
242 4 μm in width, and width peaking at ~3.3 μm, consistent with previous observations that cells
243 remain constant in width until G2 phase (2).
244
245 For the 4C gate, cell body length revealed a bimodal distribution, with peaks centred at ~7.5
246 μm and ~14.5 μm (Fig. 3B). This is likely to reflect that late S phase and early G2 phase
247 cells are long, but very rapidly shorten and widen during G2 phase and into mitosis (2). Next,
248 these peaks were gated to separate cells with cell bodies of ≤10 μm (36.6% cells; short) or
249 >10 μm (63.4% cells; long) in length (Fig 3B). The range of morphological parameters
250 described above were plotted for the long and short populations to determine whether any
251 further discrimination of these populations could be achieved. Only aspect ratio,
252 elongatedness and width offered a means of distinguishing the majority of short 4C-gated
253 cells from all other cells gated on DNA content; none of the parameters selectively
254 discriminated long 4C-gated cells (Fig 3C, S7 Fig). Again, to allow the easiest comparison
255 with previous studies, we chose to focus on width.
256
257 Both long and short 4C-gated cell populations displayed a bimodal width distribution.
258 Overall, the majority of the shorter 4C cells were wider than the longer 4C cells (Fig 3C).
259 Based on previously described *L. mexicana* promastigote morphology (2), it is likely that the
260 cells from the 4C gate with longer, narrower cell bodies comprised mostly late S/early G2

261 phase cells, while the 4C cells with shorter, wider cell bodies comprised mainly cells in late
262 G2, M phase and cytokinesis. There was some overlap in width between the long and short
263 cell populations (Fig 3C, subpeaks 2 and 3), most likely reflecting the changes to cell
264 morphology that occur during G2 phase, as well as biological variation in cellular
265 morphology. This was consistent with viewed images of the 4C cells corresponding to each
266 subpeak (Fig 3D); long, narrow cells had either one flagellum (S phase), or one long and one
267 very short flagellum (likely early G2 phase), while short, wide cells had two flagella (with a
268 longer daughter flagellum) often accompanied by evidence of cytokinesis furrow formation or
269 cleavage (G2/M/C cells). These data emphasise the pitfalls of relying on manual gating
270 alone to determine cell cycle stage solely from DNA content, since the 4C gate includes a
271 significant proportion of cells still in S phase in addition to post-S phase stages.
272

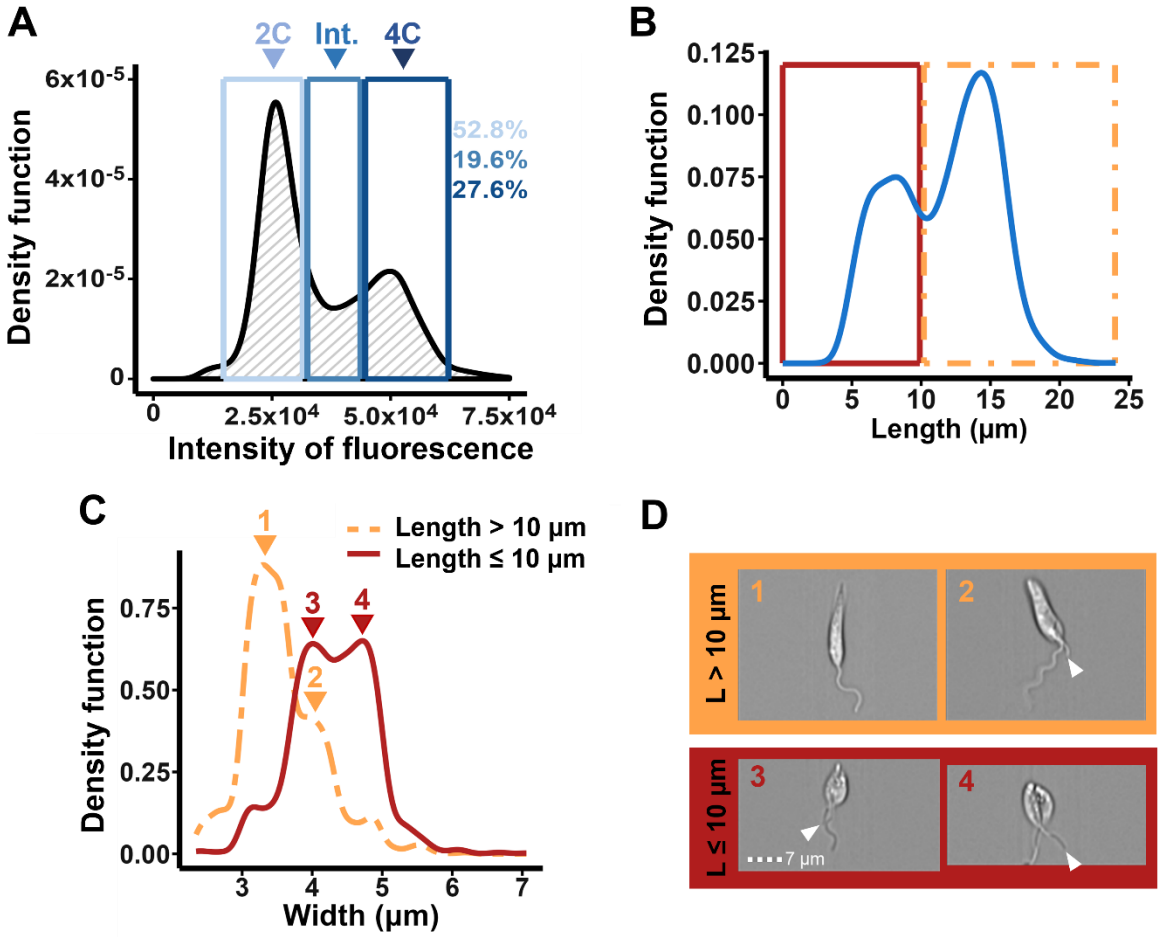

Fig 3. Distinguishing late S, G2, M and cytokinesis cells based on their DNA content and cell body parameters.

L. mexicana C9T7 promastigote cells were stained with DCO and analysed by IFC. (A) The DNA fluorescence profile previously presented in Fig 2B was manually gated using IDEAS™ software (blue boxes) to select cells with 2C, intermediate (Int.; 2C-4C) or 4C DNA content based on the peaks. (B) Plot of the cell body lengths of cells within the gated 4C population (blue line). A 10 µm cut-off was applied to separate the two peaks (red and yellow boxes). (C) Plot of the cell body widths of each of the two subpopulations identified in panel B (yellow (length > 10 µm) and red (length ≤ 10 µm), with example images from the respective peaks shown in (D). The distal end of the daughter flagellum in cells with two flagella is indicated by a white arrowhead. Scale bar: 7 µm.

285 Given the difficulties in unambiguously identifying the cell cycle stage of cells post-S phase
286 from their DNA content and cell morphology alone, the spindle-associated orphan kinesin
287 KINF was tagged at its N terminus with mNeonGreen using CRISPR/Cas9 technology in *L.*
288 *mexicana* promastigote C9T7 cells to allow the identification of cells undergoing mitosis.
289 Analysis of cells expressing mNG:KINF by immunofluorescence using an anti-mNG
290 antibody, in conjunction with the β-tubulin antibody, KMX, revealed cell cycle-dependent
291 localisation (Fig 4), consistent with a previous report of KINF localisation (45). Cytoplasmic
292 fluorescence was observed in all cells, but this was deemed to be background as similar
293 fluorescence was observed in the C9T7 parental cell line (Fig 4A) and mNG:KINF was not
294 detected in the cytoplasm when live cells were analysed by IFC (Fig 5A). In C9T7
295 mNG:KINF cells, mNG:KINF was expressed, as expected, in cells undergoing mitosis and
296 shown to colocalise with the spindle microtubules (Fig 4G,H). However, following mitosis and
297 disassembly of the spindle, mNG:KINF dispersed throughout each nucleus in 2N2K2F cells
298 as daughter cells were separated by cytokinesis (Fig 4I). Amongst 1N1K1F cells, three
299 groups of cells could be distinguished based on their mNG:KINF fluorescence and cell body
300 length. A few 1N1K1F cells with short cell bodies displayed mNG:KINF fluorescence
301 distributed across their nucleus (Fig 4B) and it is likely that these were new G1 phase cells,
302 with residual mNG:KINF fluorescence remaining after cytokinesis. Other 1N1K1F cells
303 displayed no mNG:KINF fluorescence, including cells with short (Fig 4C) or long (Fig 4D) cell
304 bodies, and likely represented cells further through G1 phase and into S phase. Additionally,
305 some long 1N1K1F cells also displayed mNG:KINF fluorescence, as a single, roughly
306 circular, focus, within the nucleus (Fig 4E) and likely represented cells later in S phase
307 starting to synthesise mNG:KINF in preparation for mitosis. 1N1K2F cells without a visible
308 mitotic spindle (G2 phase cells) also displayed mNG:KINF staining, distributed across the
309 nucleus (Fig 4F). Thus, it appears that mNG:KINF expression commences partway through
310 S phase, with the protein localising across the nucleus. mNG:KINF then localises to the
311 mitotic spindle, and following spindle disassembly, redistributes across the nuclei, persisting
312 into early G1 before, presumably, the protein is degraded.

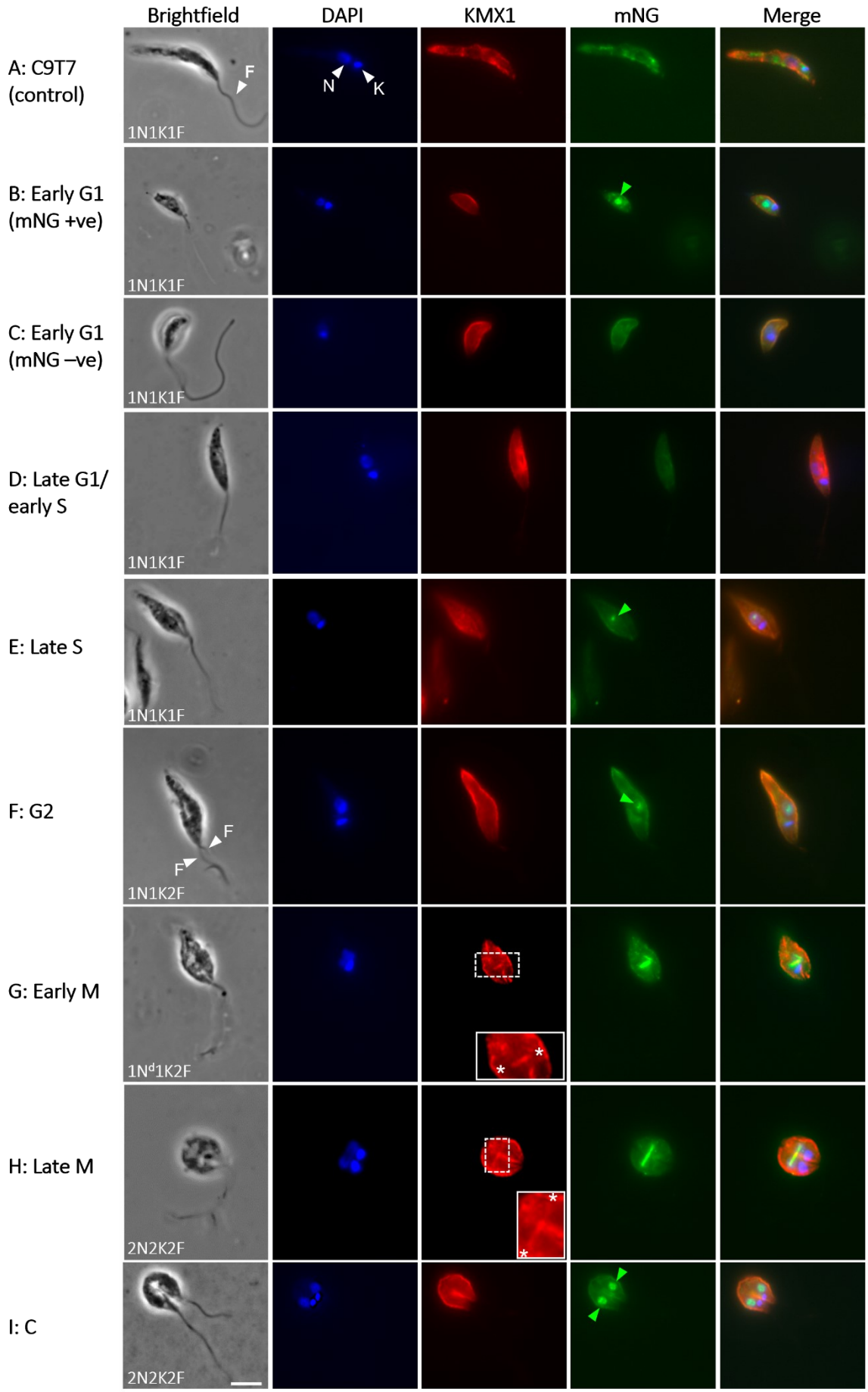
Brightfield
DAPI
KMX1
mNG
Merge
A: C9T7 (control)
B: Early G1 (mNG +ve)
C: Early G1 (mNG –ve)
D: Late G1/ early S
E: Late S
F: G2
G: Early M
H: Late M
I: C
F
N
K
1N1K1F
1N1K2F
1N^d1K2F
2N2K2F

313

314 **Fig 4. mNG:KINF displays a cell cycle-dependent localisation.**

315 Immunofluorescence was performed on *L. mexicana* promastigote C9T7 (control) (A) or C9T7
316 mNG:KINF cells (B-I) with the KMX-1 antibody to detect β-tubulin and an anti-mNG antibody to
317 detect mNG:KINF. Cells were also stained with DAPI to visualise DNA. From left to right: brightfield,
318 DAPI (blue), KMX-1 (red), mNG (green) and DAPI/KMX-1/mNG merged images. The number of nuclei
319 (N), kinetoplasts (K) and flagella (F) per cell is indicated (N^d indicates a dividing nucleus), along with
320 the cell cycle stage. White arrowheads indicate N, K and F. Dotted boxes highlight the mitotic spindle
321 as stained by the KMX-1 antibody, which is enlarged and indicated by asterisks in the non-broken
322 line boxes; green arrowheads indicate mNG:KINF staining within the nucleus. Scale bar = 5 µm.

323

324

325

326 We then sought to determine if we could automatically classify and quantify the cell cycle
327 expression pattern of mNG:KINF using IFC. In IFC images of C9T7 mNG:KINF cells, the
328 mNG:KINF fluorescence signal was masked (Fig 5A) and the number of masks (and
329 therefore discrete mNG:KINF signals) per cell was determined using the IDEAS™ spot count
330 feature. This allowed cells with no, one or two mNG:KINF foci per cell to be distinguished.
331 Further, cells with one mNG:KINF focus were expected, from immunofluorescence data to
332 possess either a roughly circular focus in their nucleus or an elongated focus on the mitotic
333 spindle (Fig 4B, E-H and Fig 5A), which could be distinguished by the aspect ratio intensity
334 (ARI) of the mask. By visual inspection of cell images, cells with an elongated mNG:KINF
335 signal (signifying mNG:KINF at the mitotic spindle) had an ARI < 0.62, while cells with a
336 circular mNG:KINF focus in the nucleus had an ARI ≥ 0.62. Thus, it was possible to
337 automatically classify C9T7 mNG:KINF cells as having a) no mNG:KINF foci (mNG:KINF-),
338 b) one circular (nuclear) focus (1CF) of mNG:KINF, c) spindle-associated mNG:KINF
339 (mitosis) or d) two circular foci (2CF) of mNG:KINF (post-mitosis) (S1C-F Table). These
340 groupings were then classified into subgroups according to their cell body dimensions
341 (length and width) to aid with cell cycle stage classification. At this stage, several anomalous
342 subgroups were identified through manual visual inspection of the cell images from each
343 group and were removed from further analysis (S1C-E Table). The largest of these
344 subgroups was a group of short, wide mNG:KINF negative cells (~5.9% total cells) that were
345 unclassifiable into any given cell cycle stage due to the mix of cells within this group; some
346 cells had morphologies consistent with being in early G1, mitosis or cytokinesis but many
347 had aberrant morphologies or appeared dead. Two groups of 2CF cells (short and narrow,
348 and long and narrow, together accounting for ~0.9% total cells) contained a small extra-
349 nuclear dot of mNG:KINF fluorescence in the region of the kinetoplast and were discarded
350 due to the aberrant fluorescence pattern, and a further group of 2CF cells (long and wide;
351 ~0.9% total cells), which were found to contain images with two cells side by side, were
352 discarded because they had been misclassified by the automatic masking. Following
353 removal of these aberrant cell groups, the average distribution of mNG:KINF staining in the

354 remaining cells was as follows: 72.4% were mNG:KINF-, 19.7% had 1CF, 6.3% had spindle-
355 shaped mNG:KINF fluorescence (mitosis) and 1.5% had 2CF (post-mitosis) (Fig 5B; S1F
356 Table).

357

358

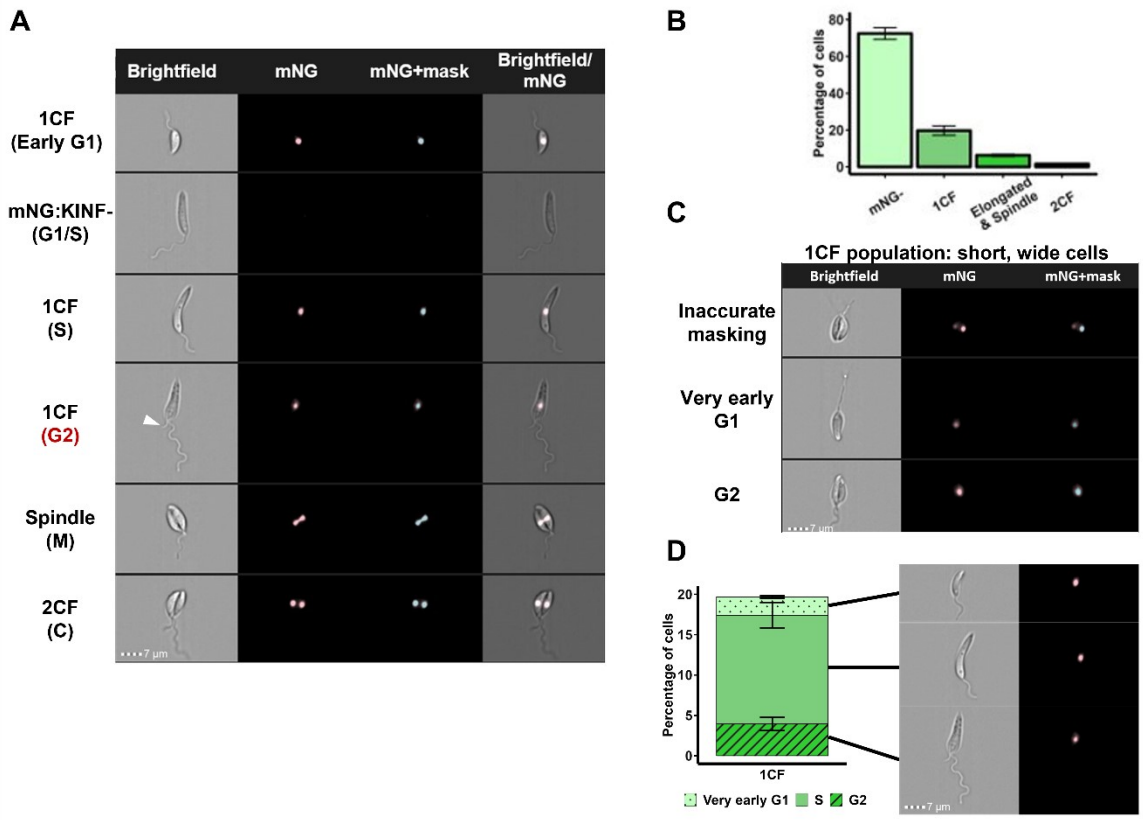

359

360 **Fig 5. Cell cycle-dependent expression and localisation of mNG:KINF facilitates the classification of**

361 **cells in G2, M and cytokinesis.**

362 (A) IFC images of live *L. mexicana* C9T7 mNG:KINF promastigote cells with differential expression of

363 mNG:KINF (from left to right: brightfield, mNG:KINF (pink), IDEAS™-applied mask (cyan) and

364 brightfield/mNG:KINF merge). The likely cell cycle stage of each example cell is indicated. A white

365 arrowhead indicates the new flagellum that has just emerged from the flagella pocket in G2 phase.

366 (B) Bar graph showing the proportions of cells displaying each expression/localisation pattern of

367 mNG:KINF. (C) Examples of short and wide 1CF cells. Top: cell showing inaccurate masking of the

368 mNG:KINF signal; such cells were subsequently reclassified as 2CF cells. Middle: cell in very early G1

369 phase (short, with 1F). Bottom: cell in G2 phase (with 2F). (D) % distribution of all cells within the 1CF

370 population after the reclassification of the post-mitotic cells as 2CF. Example images of each cell

371 type are shown. Scale bars: 7 µm. Error bars show standard deviation of the means of 3 replicates.

372

373 From visual inspection, the 2CF cells contained only post-mitotic cells. However, inspection
374 of cells classified as having mNG:KINF at the mitotic spindle, revealed a small group of long,
375 narrow cells that only possessed one flagellum (S1C-E Table). From the orientation of the
376 mNG:KINF fluorescence, which was aligned along the long axis of the cell, rather than
377 perpendicular to it as is more normal during mitosis, it was judged that this subgroup was
378 rather in S phase, with a slightly more elongated mNG:KINF signal than the majority of 1CF
379 cells (S8 Fig); thus these cells were reclassified as S phase. Within the 1CF population, it
380 was expected that there would be very early G1 phase cells with short, narrow cell bodies, S
381 phase cells with long, narrow cell bodies as well as G2 cells with a range of morphologies,
382 some of which would overlap with the morphologies of the other cell cycle stages. However,
383 while these cell types were indeed observed during visual inspection of the 1CF cell images
384 and associated cell body dimension scatter plots, an additional group of short, wide cells
385 possessing two circular mNG:KINF foci was observed (0.3 % total cells; Fig 5C, S1C-E
386 Table). For these cells, only one of the two foci had been masked, likely because the
387 second CF was in a different focal plane from the first (Fig 5C); these cells were reclassified
388 as being post-mitosis. To identify G2 cells amongst the remaining 1CF cells (19.7% total
389 cells), cell images were visually inspected for the presence of two visible flagella (Fig 5C).
390 3.9% total cells were deemed to be in G2 phase by this criterion (Fig 5D, S1C-F Table) and,
391 as predicted by previous analyses showing that post-S phase cells undergo significant
392 morphological remodelling in preparation for mitosis (2), G2 cells displayed a wide variation
393 in length and width (S9 Fig). Further, 1CF cells were judged to be in very early G1 if they
394 were short and narrow with one flagellum (2.3 % total cells) and in S phase if they were long
395 with one flagellum (13.5 % total cells) (Fig 5C, Table 1, S1C-F Table).

396

397

398

399 **Table 1 Properties of C9T7 mNG:KINF cell cycle stage populations**

Variable	Cell population							
Cell cycle stage	Very early G1	Early G1	Late G1	Early S	Late S	G2	M	Cytokinesis
NKF configuration	1N1K1F	1N1K1F	1N1K1F	1N1K1F	1N1K1F	1N1K2F	$1N^d1K2F$	2N2K2F
DNA content	2C	2C	2C	~2C-3C	~3C-4C	4C	4C	4C
Cell body length (µm)	≤10	≤10	>10	>10	>10	any	≤10	≤10
Cell body width (µm)	<4	<4	<4	<4	<4	any	≥4	≥4
mNG:KINF status	positive	negative	negative	negative	positive	positive	positive	positive
mNG:KINF pattern	1 circular focus	n/a	n/a	n/a	1 circular focus	1 circular focus	spindle	2 circular foci
% population	2.3	17.7	27.9	27.0	13.4	3.9	6.1	1.7
Duration of cell cycle stage	12 mins (0.20 hrs)	1 hr 40 mins (1.67 hrs)	3 hrs 1 mins (3.02 hrs)	3 hrs 30 mins (3.5 hrs)	2 hr 2 mins (2.03 hrs)	38 mins (0.64 hrs)	1 hr 2 mins (1.03 hrs)	19 mins (0.31 hrs)
Cumulative time through cell cycle	12 mins (0.20 hrs)	1 hr 52 mins (1.87 hrs)	4 hrs 53 mins (4.88 hrs)	8 hrs 23 mins (8.38 hrs)	10 hrs 25 min (10.41 hrs)	11 hrs 3 mins (11.05 hrs)	12 hrs 5 mins (12.08 hrs)	12 hrs 23 mins (12.39 hrs)
Duration in unit cell cycle stage	0.016 U	0.135 U	0.243 U	0.282 U	0.164 U	0.052 U	0.083 U	0.025 U
Cumulative time through unit cell cycle	0.016 U	0.151 U	0.394 U	0.677 U	0.841 U	0.892 U	0.975 U	1 U

400

401 Based on mNG:KINF expression and localisation, cell morphology and DNA content, C9T7 mNG:KINF
402 cells were classified into different cell cycle populations. The proportions of cells in each of the cell
403 cycle populations was then used to calculate the duration of that stage. Cumulative time through the
404 cell cycle was also calculated up to the end of each cell cycle stage using Williams' analysis (46).
405 Absolute timings were also converted to a proportion of the unit cell cycle, where cell cycle progress
406 is scaled to between 0 and 1. N: nucleus; K: kinetoplast; F: flagellum; 2C, 3C and 4C: DNA content; U:
407 units.

408

409 Similarly, within the mNG:KINF- population, early G1 cells were identified through their short,
410 narrow cell bodies (17.7% total cells), but the remainder (late G1 and early S phase cells;
411 55.0% total cells) could not be separated on their morphological features because they both
412 had similarly long cell bodies (Table 1, S1C-E,H Table). Therefore, we looked to distinguish
413 them using DNA content. On analysis of mNG:KINF cells stained with DCO, it was apparent
414 this combination of fluorescence was unsuitable; although mNG and DCO fluorescence are
415 both excited by a 488 laser, they emit in different channels of the imaging flow cytometer, but
416 their optimal excitation required very different laser powers (3 mW for DCO and 120mW for
417 mNG:KINF). Therefore, KINF was tagged with mCherry which is excited by a 561 nm laser,
418 in an attempt to allow simultaneous determination of DNA content using DCO staining.
419 However, the resultant mCherry:KINF fluorescent protein was not bright enough to be
420 detected by IFC. Instead, a second aliquot of the C9T7 mNG:KINF cells analysed for
421 mNG:KINF fluorescence was stained with DCO and excited with the 488 nm laser at 3 mW.
422 This enabled the detection of DCO staining in C9T7 mNG:KINF cells without exciting
423 detectable mNG:KINF fluorescence, enabling the quantification of cellular DNA content by
424 applying manual 2C, intermediate (2C-4C gate) and 4C gates (see example plot in S10 Fig
425 and data for three replicates in S1G,H Table). Given the overlap of G1 and S phase cells
426 within the 2C and intermediate gates (S6A,B Fig), a precise determination of the proportions
427 of non-fluorescent G1 and S phase cells was not possible. However, by subtracting the
428 proportions of early G1 cells (determined from their morphology and mNG:KINF
429 fluorescence (short cell bodies with either one mNG:KINF focus (2.25 %) or no mNG:KINF
430 fluorescence (17.65%)) from the average percentage of cells in the 2C gate obtained from
431 DCO staining of C9T7 mNG:KINF cells (47.8%), it can be estimated that within the
432 mNG:KINF- population, 27.9% cells are in G1 phase. Subtracting this value from the 55.0%
433 of combined G1/S mNG:KINF- long cells indicated that 27.0% total non-fluorescent cells
434 were in S phase (Table 1, S1H Table).

435 The resultant percentages allowed the durations of the various cell cycle stages to be
436 calculated (2, 46) for the C9T7 mNG:KINF cell line based on its doubling time of 12 hours 23
437 minutes (12.4 hours) (Table 1). Cell cycle timings were also converted to a fraction of the
438 unit cell cycle (where progress through the cell cycle is scaled to between 0 and 1). This
439 showed that G1 phase lasted for ~4.9 hours, S phase for ~5.5 hours, G2 phase for just 38
440 minutes (0.64 hrs), mitosis for ~1 hr and the post-mitotic period for 19 minutes (0.31 hrs),
441 equating to 0.4, 0.45, 0.05, 0.08 and 0.03 of the unit cell cycle, respectively, consistent with
442 the unit cell cycle values calculated by Wheeler et al, 2011 (2). This is the first determination
443 of the length of G2 and the post-mitotic period in *L. mexicana.* A precise timing for
444 cytokinesis was not possible from our data, since visual inspection of the mitotic and post-
445 mitotic populations showed that in the majority of cases, the formation and cleavage of the
446 furrow began during mitosis (Fig 6). A few mitotic cells were observed without a visible
447 furrow (Fig 6A), but it could not be ruled out that this was due to their orientation in the
448 images. However, it is clear from our analysis that cytokinesis commences early in mitosis
449 and continues beyond the completion of mitosis. Cell cleavage appeared to mostly begin at
450 the anterior end (the flagella end) of the cell, but some cells showed cleavage occurring
451 bidirectionally from each end (Fig 6). The cell cycle timings also revealed that mNG:KINF
452 expression commenced ~60% of the way through S phase (8.4 hrs or 0.68 U into the cell
453 cycle) with mNG:KINF being present for the remainder of the cell cycle before being
454 degraded very rapidly, 12 minutes into the new cell cycle. These data provide a more
455 detailed set of timings of the different cell cycle stages in promastigote *L. mexicana* as
456 shown in the scaled schematic in Fig 7.

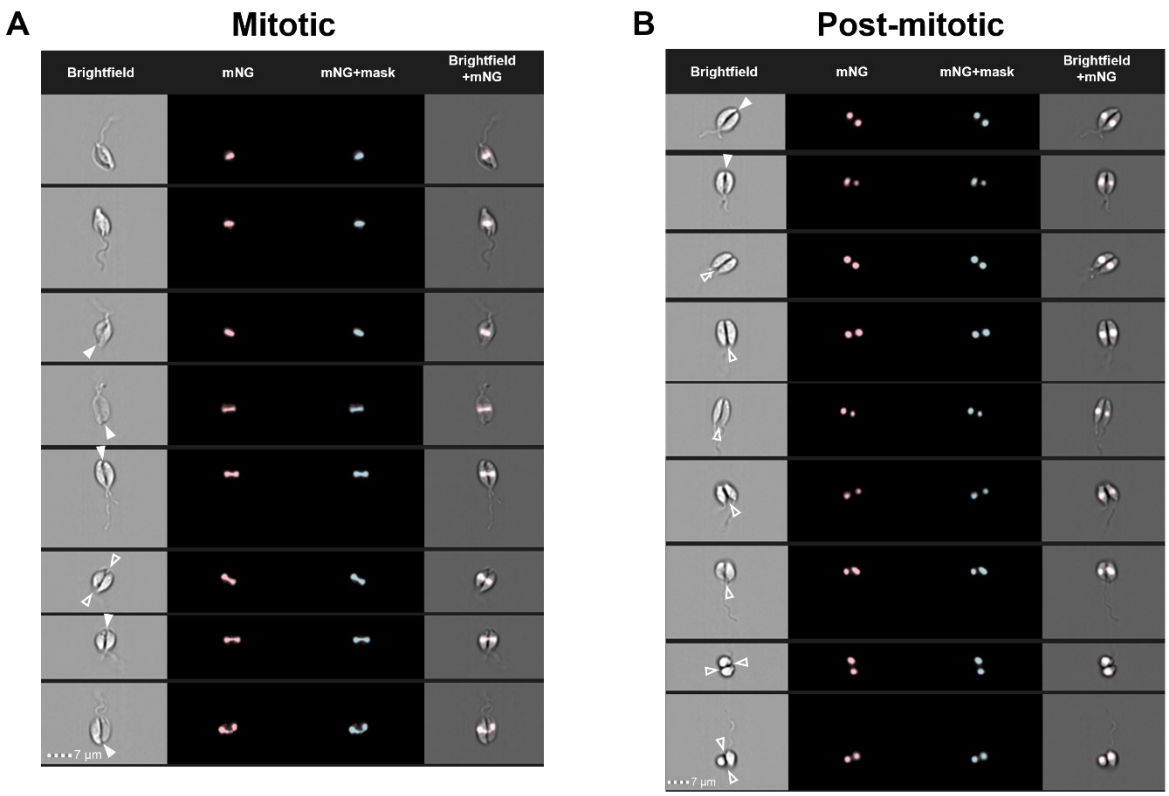

Fig 6. Cytokinesis begins early during mitosis.

Images of (A) mitotic and (B) post-mitotic C9T7 mNG:KINF cells, as determined from their mNG:KINF fluorescence pattern, showing the formation of a furrow (closed arrowheads) and cell cleavage (open arrowheads). Scale bars: 7 µm.

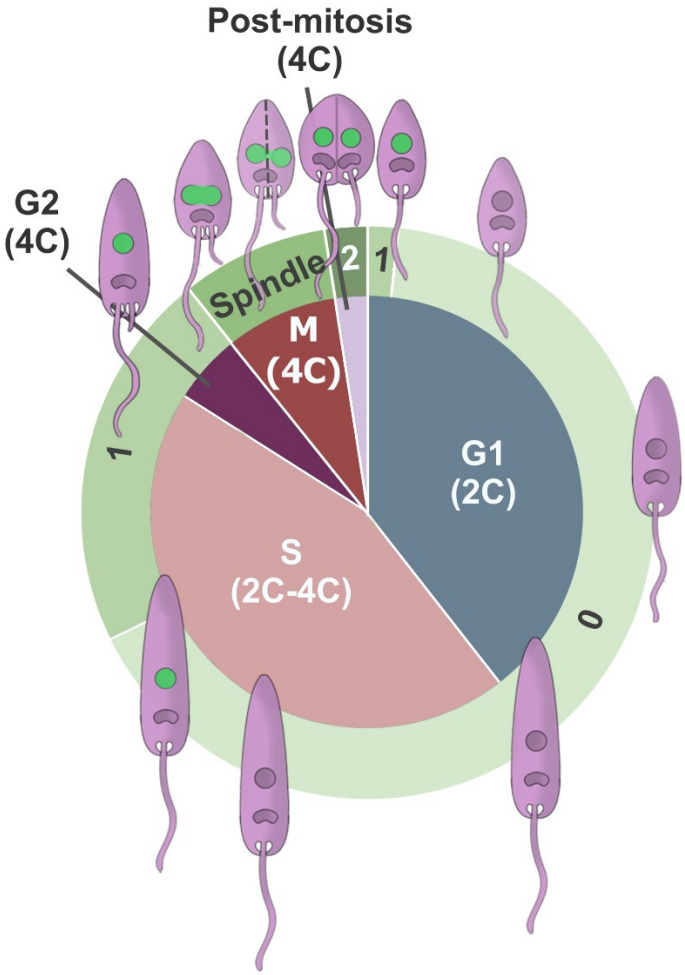

Figure 7. Schematic of the *L. mexicana* cell cycle

The inner circle shows the five main stages of the cell cycle, scaled according to their duration, along with the DNA content of cells progressing through those stages. The outer circle indicates the cell cycle-dependent expression of mNG:KINF, either to circular foci within the nucleus (1 or 2) or to the mitotic spindle. The '0' indicates cells with no mNG:KINF expression. Cartoons of cells at each cell cycle stage showing the cell body and flagella (light purple), nuclei and kinetoplasts (dark purple), and forming furrow (dotted and solid lines) are indicated on the outside. mNG:KINF nuclear fluorescence is in green.

475 **Discussion**

476

477 Much of our current knowledge of *Leishmania* cell cycle events and their order and duration
478 derives from studies where fixed promastigote parasites have been analysed manually by
479 fluorescence microscopy (2, 4, 6, 8, 47). DNA dyes are commonly used to visualise and
480 enumerate the nuclei and kinetoplasts or thymidine analogues such as BrdU (5-bromo-2`-
481 deoxyuridine) or EdU (5-ethynyl-2`-deoxyuridine) to detect DNA synthesis.
482 Immunofluorescence of cytoskeletal proteins may aid visualising and documenting organelle
483 replication, and cell morphology is generally assessed under phase contrast and may be
484 supplemented with electron microscopy to analyse the structural detail of cells. Cell
485 morphological parameters such as cell body or flagellum length and width may be measured
486 and DNA content measurements performed on individual cells using software such as
487 ImageJ (48, 49). While there is no doubt that such studies are often very detailed and
488 carefully performed, the laborious nature of manual analyses have limited the numbers of
489 cells able to be analysed to a few hundred, at most, per replicate (2, 4). Often, microscopy
490 is supplemented with flow cytometry analysis of total cellular DNA content of PI-stained cells
491 (6), which, while offering greater throughput (tens of thousands of cells analysed per
492 replicate), does not provide data on how many organelles are in each cell, and only limited
493 information about cell size and shape.

494

495 High throughput analysis of microscopy images (of fixed or live cells, stained with DNA dyes
496 and/or expressing fluorescently tagged proteins) has also been developed for kinetoplastids,
497 using ImageJ scripts to automate measurement of DNA content and nucleus and kinetoplast
498 number per cell, cell length, width, shape and the position of nuclei and kinetoplasts along
499 the long axis of the cell (44, 50). Further, the nuclei and kinetoplasts in *L. mexicana* and the
500 related kinetoplastid, *Trypanosoma brucei*, can be differentially stained with different DNA
501 dyes (44, 51). Base-pair intercalators (BPIs) such as PI and SybrGreen, do not have any
502 particular sequence specificity and so stain the nucleus, which contains more DNA, more

503 brightly than the kinetoplast. In contrast, minor groove binding dyes (MGBs), such as DAPI
504 (4`, 6-diamidino-2-phenylindole) and Hoechst 33342, have a greater affinity for A-T-rich DNA
505 and therefore preferentially stain kinetoplast DNA over the nuclear DNA. Co-staining with
506 one BPI and one MGB dye allows, following chromatic aberration correction and colour
507 deconvolution of acquired fluorescent images, the automated detection of nuclei and
508 kinetoplasts, and the separate measurement of their DNA content using ImageJ (44).
509 However, this approach requires that cells are imaged on microscope slides prior to ImageJ
510 analysis, with both sample/slide preparation and image capture being critical for accuracy
511 and consistency and, potentially, rate-limiting.
512
513 Here, we have developed new cell cycle analysis pipelines for live *L. mexicana*
514 promastigotes in solution that require only minimal manipulation (washing, staining (if
515 required) and resuspension in PBS) of the parasites prior to their analysis by IFC. Imaging
516 cells live and in solution offers several advantages over imaging cells on microscope slides.
517 Fixation artefacts are not introduced, cells cannot dry out and cell morphology is not altered
518 by coming into contact with a surface. The throughput of IFC greatly surpasses that of
519 microscopy, with tens of thousands of cell images and dozens of parameters for each image
520 being captured in as little as 5 minutes. Being able to view brightfield and fluorescence
521 images of every cell analysed, and to automatically quantify their many parameters without
522 needing to write custom scripts, offers hereto unparalleled insights into the *Leishmania* cell
523 cycle, and provides far greater consistency of analysis than has been possible to date with
524 other methods. Additionally, because IFC captures all possible brightfield and fluorescent
525 parameters for every cell image at the outset, this permits backtracking during analysis to
526 explore additional parameters for any given cell, even if these were not part of the initial
527 experimental design, as well as to visually verify gated cells, and, as we have done here, to
528 supplement automatically acquired data with manual analysis, thereby providing enormous
529 flexibility.
530

531 To be able to take advantage of all that IFC has to offer, we first had to find a DNA dye that
532 was quantitative in live *L. mexicana* cells. The BPI, PI, is quantitative (S2A,B Fig), but can
533 only be used in fixed, RNAse-treated cells due to it being non-membrane permeable and
534 also binding to RNA. Despite the MGB Hoechst 33342 being widely used to stain DNA in
535 live *Leishmania*, it was not quantitative under the conditions used here (S2C Fig), which was
536 surprising because Hoechst is a quantitative stain for live *T. brucei*. However, examination
537 of images of cells stained with Hoechst showed that they also displayed regions extra-
538 nuclear fluorescence, suggesting that Hoechst staining was not restricted to the nucleus.
539 The BPI, DRAQ5, in contrast, appeared visually to label only the nucleus (S2D Fig), but still
540 was not quantitative. While the DNA binding mechanisms of the Vybrant Dye Cycles are to
541 our knowledge, not known, DCV appeared to specifically label both the nucleus and
542 kinetoplast, with brighter staining of the kinetoplast, suggesting it might be an MGB.
543 However, it was also not quantitative (S2E Fig), despite being so in *T. brucei* bloodstream
544 form cells (52). DCR also was not quantitative, staining both the nucleus and kinetoplast,
545 but also throughout the cytoplasm (S2F Fig) under the conditions tested. However, we found
546 a third Vybrant DyeCycle dye, DCO, previously reported to be quantitative in procyclic for *T.*
547 *brucei* (53), was quantitative at a much lower concentration (0.625 μM) in promastigote *L.*
548 *mexicana* than that used for *T. brucei* (5 μM), provided cells were imaged promptly after
549 staining (Fig 2, S4 Fig). We also showed it to be non-toxic under the conditions used (S3
550 Fig), which is important given that DCO, along with DRAQ5 and Hoechst 33342, were
551 reported to display cytotoxicity and cause G2/M arrest in HeLa cells (54, 55). DCO stained
552 both DNA-containing organelles, preferentially labelling the kinetoplast, suggesting it may be
553 an MGB. Since S phase of the nucleus and kinetoplast are synchronous in *L. mexicana*
554 promastigotes, this dye worked well to determine relative DNA content of cells throughout
555 the cell cycle, providing comparable data to PI (Fig 2, S2A,B Fig), although the preferential
556 binding to kDNA should be borne in mind in the event of analysing DNA content under
557 conditions where DNA synthesis of one of these organelles is preferentially affected.
558

559 Staining live *Leishmania* with DCO before imaging with IFC not only allowed a cell's DNA
560 content to be determined, giving an approximation of its cell cycle position, but also to be
561 matched to its morphology, allowing greater level of automatic discrimination of some cell
562 cycle stages, e.g., cells in G1 phase (2C gate) could be split into early and late G1 cells on
563 the basis of their length. However, distinguishing late S phase cells from early G2 cells, or
564 late G2 cells from mitotic cells was not possible from their DNA content and cell body
565 length/width due to their identical DNA content and overlapping dimensions. To delineate the
566 start and end of G2 phase, we employed fluorescent labelling of the orphan spindle kinesin,
567 KINF, to detect spindle formation at the start of mitosis and disassembly at the end of
568 mitosis. Serendipitously, we found that mNG:KINF expression and localisation allowed us to
569 also identify mid-S phase-G2 cells (one circular focus, long cells), post-mitotic cells in the
570 latter stages of cytokinesis (2 circular foci in short, wide cells) and newly divided cells (one
571 circular focus, short, narrow cells). We were then able to distinguish late S phase and early
572 G2 phase cells by examining images of these cells to determine whether a second daughter
573 flagellum had emerged from the flagellar pocket. Although we performed this manually in
574 this study, we believe this should be possible to automate by, for example, fluorescently
575 tagging the axoneme capping structure protein (ACS1; (56)) at the distal tip of the flagellum
576 and using the IDEAS™ spot count feature to distinguish between one and two ACS1 foci.
577 However, to combine ACS fluorescence with mNG:KINF may, depending on its brightness,
578 require a tag other than mCherry, which we found when tagged to KINF was not detectable
579 by IFC. The recently developed mScarlet3 (57), or perhaps a cyan fluorescent protein (58)
580 may provide an alternative that also permits co-staining and analysis with DCO.
581
582 Being able to distinguish cells in different cell cycle stages allowed the calculation of their
583 duration and allowed us to determine the length of the G2, mitosis and post-mitosis phases
584 separately for the first time (Table 1). While the doubling time of our C9T7 mNG:KINF cell
585 line (12. 4 hrs) is considerably longer than that of the wildtype WHO strain
586 MNYC/BZ/62/M379 cell line (7.1 hrs) used by Wheeler *et al.*, (2), the unit cell cycle durations

587 of the pre-S (0.40 U), S (0.45 U) and post-S (0.16) phases we determined are highly
588 consistent the equivalent ranges reported by Wheeler *et al*., from four different analysis
589 methods (pre-S: 0.35-0.4; S: 0.4-0.49; post-S: 0.14-0.22). Further, we provide much greater
590 resolution of cell cycle stages, being able to distinguish three stages of G1 phase (newly
591 divided cells, early and late G1), early and late S phase, G2 phase, mitosis and post-mitosis
592 (Table 1). Of particular note is the ability, because of the high-throughput nature of IFC, to
593 detect reliably cells in short-lived cell cycle stages, for example, new cells within the first 12
594 minutes of the cell cycle (2.3% cells), G2 phase (38 minutes; 3.9% cells) and post-mitotic
595 cells (19 minutes; 1.7% cells). Further, being able to view sufficient numbers of cells in rarer
596 cell cycle stages may negate the need to use enrichment techniques such as cell cycle
597 synchronisation with agents such as hydroxyurea or flavopiridol (6, 59-61). Additionally, we
598 were able to demonstrate that cytokinesis likely commences in early mitosis (Fig 6), with
599 new membrane, and presumably also the subpellicular microtubules of the cleavage furrow
600 forming in cells where mNG:KINF fluorescence shows there is still a mitotic spindle present.
601 Cell cleavage appears to commence at the anterior end of the cell body and proceed
602 towards the posterior in most cells, but a number of cells could be observed with cell
603 cleavage occurring bidirectionally from each end of the cell, indicating some differences
604 compared to cytokinesis in the related kinetoplastid, *T. brucei* (62, 63).
605
606 Overall, our application of IFC to studying the cell cycle in *Leishmania* provides an extra
607 dimension to the growing body of IFC applications for studying the cell biology of parasites.
608 IFC has been used to assess morphological changes occurring during promastigote to
609 amastigote differentiation in *L. donovani* (64), to assess colocalisation of mCLING and
610 lysotracker fluorescent stains in *T. brucei* (32) and to assess PI live/dead staining and for
611 morphological measurements in *L. mexicana* (34). IFC has also been employed extensively
612 to study host-parasite interactions for *Leishmania* and other intracellular pathogens) (19, 65-
613 68) as well as to detect *Leishmania* infections in blood and parasite dissemination to organs
614 around the body (69). It has also been used to study trogocytosis by *Entamoeba histolytica*

615 (70) and for drug screening in *Plasmodium falciparum* (71). The huge flexibility and high-
616 throughput nature of IFC provide opportunities to study the cell biology of parasites such as
617 *Leishmania* at a scale and level of detail that hitherto has not been possible. The cell cycle
618 analysis pipelines we have developed here should, for example, provide the means to
619 identify and extensively characterise cell cycle and morphological perturbations in mutant or
620 drug-treated cell lines, to study the expression and localisation of proteins of interest
621 throughout the cell cycle and to identify rare phenotypes that only occur in a small subset of
622 cells. Furthermore, IFC provides a simple method of automated image capture for live cells,
623 reducing artefacts and experimental variation, as well as standardised and largely
624 automated image analysis that allows the visual insights of microscopy to be linked with the
625 high-throughput quantitation of flow cytometry for every individual cell, providing a step
626 change for *Leishmania* cell cycle analysis.
627
628
629 **Materials and methods**

630 ***Leishmania* cell culture**

631 *Leishmania mexicana* M379 Cas9 T7 (C9T7; (72)) promastigote cells were cultured in
632 medium 199 (M199; (73)) supplemented with 10% foetal bovine serum (FBS), 32 μgml^{-1}
633 hygromycin and 50 μgml^{-1} nourseothricin sulphate at 27ºC. All analyses were conducted
634 using cells grown to mid-log phase ($1x10^6$ – $7x10^6$ $cellsml^{-1}$).

635 **Generation of an mNG:KINF tagged cell line**

636 The spindle-associated orphan kinesin F (KINF; LmxM.25.1950) was tagged with
637 mNeonGreen (mNG) at its N-terminus using CRISPR-Cas9 technology (73). PCR was
638 performed to generate the sgRNA and DNA donor templates with primers designed using
639 LeishGEdit (http://www.leishgedit.net/) [upstream forward primer: 5`-
640 TCGTTCTCTCCGTCTCTCGGGGTGGCTGCCgtataatgcagacctgctgc-3`, upstream reverse

641 primer: 5`-TACCGCCACCTTGATGCTAGACGACGACATactacccgatcctgatccag-3` and 5'
642 sgRNA primer: 5`-
643 aaattaatacgactcactataggCTCCTTGCACCAGCAAAGACgttttagagctagaaatagc-3`] as well as
644 the common sgRNA scaffold primer G00, and the pPLOTv1 blast-mNeonGreen-blast
645 plasmid (72) as DNA template. C9T7 cells were transfected with the amplified templates and
646 tagged cell lines were selected and cloned as described by (73). The expression of
647 mNG:KINF was confirmed and analysed by fluorescence microscopy and IFC.

648 **Immunofluorescence**

649 1 x 10^7 *L. mexicana* promastigote mid-log phase cells were washed with phosphate buffered
650 saline (PBS), fixed with 4% paraformaldehyde for 15 mins at room temperature (RT) and
651 washed again in PBS before being permeabilised in 4% bovine serum albumin (BSA)
652 containing 0.075% Tween-20 for 10 mins at RT. Cells were then sequentially incubated in
653 mouse anti-mNeonGreen (IgG2c; Chromotek), followed by rat anti-mouse IgG(H+L)-
654 AlexaFluor488 (ThermoFisher), mouse anti-KMX-1 (IgG2b; Millipore Merck) and then goat
655 anti-mouse IgG2b(Fcγ)-AlexaFluor594 (ThermoFisher), each for 2 hours at RT. Each
656 antibody was diluted 1:500 in 4% BSA/0.075% Tween-20, and cells were washed twice with
657 PBS between each antibody addition. After the final antibody was washed off, cells were
658 resuspended in PBS and stored at 4°C in the dark. Before imaging, Fluoroshield™ with
659 DAPI (Sigma) was added to the cell suspension before mounting on poly-L-lysine-coated
660 glass slides. Imaging was performed with a Zeiss Axio Observer 3 microscope and ZEN
661 Blue software (Zeiss). Images were processed with ImageJ version 2.9.0 (74).

662 **Imaging flow cytometry (IFC)**

663 For IFC of live, unstained cells, ~5 x 10^6 *L. mexicana* promastigote cells were washed and
664 then resuspended in 60 µl PBS. Alternatively, live cells were first resuspended in 1 ml M199
665 medium or PBS and stained in the dark with Hoechst 33342 (1 $\mu g ml^{-1}$ for 10 minutes at RT),
666 Vybrant™ DyeCycle™ Orange (DCO; 0.625 µM for 30 minutes at RT), Vybrant™

667 DyeCycle™ Violet (DCV; 40 μM for 15 minutes at 27ºC), Vybrant™ DyeCycle™ Ruby (DCR;
668 12.5 μM for 15 minutes at 27ºC) or with DRAQ5™ (Invitrogen; 25 μM for 15 minutes at RT),
669 before being harvested and resuspended in 60 μl PBS. To fix cells, *L. mexicana* were
670 washed in PBS and incubated in either 4% paraformaldehyde (PFA) in PBS for overnight at
671 4ºC, or in ice-cold 70% methanol/30% PBS overnight at 4ºC. To stain methanol-fixed cells
672 with propidium iodide, cells were washed in PBS/5 mM ethylenediaminetetraacetic acid
673 (EDTA) and resuspended in 500 μl PBS/5 mM EDTA/10 μgml^{-1} propidium iodide/20 μgml^{-1}
674 RNAse A and incubated at 37ºC for 45 minutes in the dark. All fixed cells were resuspended
675 in 60 μl PBS just prior to being analysed by IFC. Prepared cells were loaded onto an Amnis®
676 ImageStream®X Mk II imaging flow cytometer (Cytek Biosciences) alongside 1 μm diameter
677 SpeedBeads (Amnis) and analysed using INSPIRE™ acquisition software. At least 10,000
678 events were captured in brightfield (BF) and fluorescence modes at 60X magnification for
679 each sample using laser colour and power settings appropriate for the relevant dye. Cell
680 data were analysed using the post-acquisition IDEAS™ software version 6.0 (75) and with
681 FCS Express™ version 7.10.0007 (DeNovo software by Dotmatics) for cell cycle modelling.

682 *Gating strategy*

683 A gating strategy (S11 Fig) was employed to identify single cells and gate out doublets,
684 debris and images with artefacts (e.g. images containing SpeedBeads, out of focus cells,
685 incorrect masking (see below), cell rosettes or more than one cell). Gates were placed
686 accordingly following visual inspection of ≥ 100 cells corresponding to individual points on
687 the relevant plots. *Leishmania* cells and then singlets were identified from cell body area
688 (calculated *via* the application of a cell body mask (see below) versus side scatter and cell
689 body area versus aspect ratio (AR) plots, respectively. The aspect ratio (minor axis/major
690 axis) of each cell body mask was calculated by IDEAS™ by applying an ellipse of best fit
691 around the mask and determining the longest and shortest dimensions (major and minor
692 axes, respectively). Out of focus images were excluded by gating for cells with a high
693 gradient root mean square (RMS; a measure of pixel contrast), the IDEAS™ Spot Count

694 feature allowed the exclusion of images containing multiple cell masks, and images
695 containing overlapping cells were excluded using cell body area versus compactness plots.

696 For DCO-labelled cells, further gating was undertaken to include only cells with high enough
697 fluorescent intensity to have successfully taken up the stain (S12A Fig). For mNG:KINF
698 tagged cell lines, additional gating was performed to identify and mask those cells
699 expressing mNG:KINF at above background levels. An mNG:KINF negative gate was placed
700 by first analysing untagged cells, before an mNG:KINF positive gate was drawn around
701 mNG:KINF tagged cells with higher fluorescence (S12B Fig). The mNG:KINF fluorescent
702 signal was then masked, as described below, to enable automatic determination of its
703 shape.

704 *Generation of masks*

705 Masks were generated for the cell body (excluding the flagellum) to allow calculation of its
706 length, width and area (Fig 1B,C), and also for mNG:KINF nuclear staining to allow
707 automatic classification of the staining pattern. The cell body mask was generated from the
708 pre-defined brightfield mask in IDEAS™, using an Adaptive Erosion Coefficient of 71 and an
709 area range of >50 pixels (equivalent to 5.56 μm^2). IDEAS™ measures the longest length of
710 the cell body mask at its midline (length) and, using the Thickness Max feature, from the
711 midline to the widest point of the mask (half maximum width), which was then doubled to
712 give the maximum width. As the resolution of measurements was 1 pixel, which equated to
713 0.33 µm for length and 0.66 µm for width, random noise was added to the data to smooth
714 these measurements. To do this, the data was extracted from IDEAS™ and imported into
715 RStudio (R version 4.0.2), where a random value between -0.33 and 0.33 µm for each
716 length measurement, or between -0.66 and 0.66 µm for each width was added to each data
717 point, before violin plots of the data were generated.

718 A mask of the mNG:KINF staining was generated using the IDEAS™ Intensity function to
719 identify pixels with a raw intensity of >100. The IDEAS™ spot count feature was used to

720 determine the number of masks per cell, and the aspect ratio intensity (ARI; minor axis
721 intensity/major axis intensity) was used to distinguish between circular masks and spindle-
722 shaped masks, which were determined visually to have ARIs of ≥0.62 and <0.62,
723 respectively.

724 *Parameters analysed*

725 The following parameters were automatically measured by IDEAS™: area (of mask; μm^2),
726 aspect ratio, brightfield intensity (sum of the intensity of the pixels within a mask, with the
727 background subtracted), circularity (which measures the degree of the mask's deviation from
728 a circle), compactness (similar to circularity but measures all pixels and takes intensity into
729 consideration), height and width (calculated by drawing a rectangular box around the cell
730 and measures its longest and shortest dimensions, respectively), elongatedness
731 (height/width), thickness_min/max (double the distance from the midpoint of the cell to the
732 perimeter at the narrowest/widest point of the cell), length, shape ratio
733 (thickness_min/length), diameter (assumes the object is a circle and calculates the diameter
734 using the area, defined as $2 \times \sqrt{(Area/\pi)}$ and the perimeter (of mask, μm).

735 **Cell cycle analysis**

736 Images of triplicate populations of *Leishmania* C9T7 and C9T7 mNG:KINF promastigote
737 cells stained with DCO were captured by IFC using a laser power of 3 mW, which allowed
738 the detection of DCO but was not sufficient to excite mNG:KINF to detectable levels. Gating
739 was performed as described above and DNA content was examined by plotting a histogram
740 of DCO intensity. Gates were drawn manually around the 2C, intermediate (>2C but <4C)
741 and 4C peaks, with the resultant data averaged for the three replicates. Cells were further
742 classified by their morphology into either long (L; >10 μm) or short (S; ≤10 μm) and wide (W;
743 >4 μm) or narrow (N) (≤ 4 μm) to allow more precise cell cycle stage identification, using the
744 morphological analysis of Wheeler *et al*., 2011 (2) as a guide. Short cells from the 2C gate
745 were reasoned to be in early G1 phase, while long 2C gated cells were in late G1 phase or

746 early S phase. Long cells in the 4C gate were deemed to be towards the end of S phase or
747 in early G2 phase, while short 4C gated cells were in late G2 phase, mitosis or cytokinesis.
748 Long cells from the intermediate DNA content gate were judged to be mostly in S phase,
749 albeit with some overlap with late G1 and early G2 cells. Additionally, G2 cells (two visible
750 flagella) were distinguished from late S phase cells (one visible flagellum) by manually
751 determining the number of flagella per cell from IFC brightfield images.

752 A second aliquot of C9T7 mNG:KINF cells, unstained with DCO, was analysed by IFC using
753 a laser power of 120 mW to permit detection of mNG:KINF. Here, gating was performed as
754 described above and cells were classified according to the fluorescence pattern observed:
755 no fluorescence, one, roughly circular, focus of fluorescence across the nucleus, one
756 elongated focus on the mitotic spindle or two circular foci of fluorescence, one in each of the
757 nuclei present in cells with two nuclei) (S12B Fig). These data were combined with
758 morphological parameters (the length of the cell body and the number of flagella visible in
759 brightfield images) to provide a more precise assessment of the cell cycle stage of individual
760 cells. Short cells with one circular focus of nuclear mNG:KINF fluorescence were deemed to
761 be in very early G1 phase while short cells with no mNG:KINF fluorescence were slightly
762 later (but still early) in G1 phase. Long cells with no mNG:KINF fluorescence were either in
763 late G1 or S phase, while long cells with a circular focus of mNG:KINF in the nucleus were
764 either in S phase or G2 phase, distinguishable by the number of visible flagella per cell.
765 Short wide cells with an elongated, spindle shaped focus of mNG:KINF fluorescence were
766 deemed to be undergoing mitosis, while short wide cells with two nuclei and mNG:KINF
767 fluorescence distributed across both of them had completed mitosis and were undergoing
768 cytokinesis. Three additional unexpected populations were also detected: short wide cells
769 with no mNG:KINF fluorescence (5.9% total cells), long wide cells with two circular
770 mNG:KINF foci (0.9% total cells) and short narrow cells, also with two circular mNG:KINF
771 foci (0.7% total cells). Upon visual inspection of the cells within these populations, the short
772 wide non-fluorescent cells were found to display a wide range of cell body morphologies,

773 many of them aberrant (S13A Fig). The long wide population with two mNG:KINF foci were
774 found to mainly contain two cells located close together that had erroneously been classified
775 as a single cell (S13B Fig), and in the short narrow population with two mNG:KINF foci, one
776 foci was found to be much smaller than usual, suggesting additional mNG:KINF
777 fluorescence in the region of the kinetoplast, independent of their cell cycle stage (S13C
778 Fig). All of these cell populations were discarded from further analysis.

779 Since cells in late G1 and S phase are of similar length, and the DNA content of late G1 and
780 early S phase cells is practically indistinguishable, in long cells with no mNG:KINF
781 fluorescence, an estimate of the distribution of these cells between late G1 and S phase was
782 made using intensity profiles of DCO fluorescence in DCO stained C9T7 mNG:KINF cells.
783 The percentage of 2C gated cells was calculated, before the percentages of short cells in
784 early S phase (with or without mNG:KINF fluorescence, obtained from IFC of non-DCO
785 stained mNG:KINF cells, as described above) were subtracted, leaving an estimate of cells
786 in late G1 phase. This was then subtracted from the total percentage of long cells with no
787 mNG:KINF fluorescence to provide an estimate of the proportion of S phase cells with no
788 mNG:KINF fluorescence.

789 Cell cycle timings were calculated using the following equation (2, 46):

791 $$\boldsymbol{x = t\frac{\ln(1 - \frac{1}{2}y)}{-\ln(2)}}$$

790

792 where x = time through the cell cycle, t = doubling time of the population and y = cumulative
793 proportion of cells up to and including that stage of the cell cycle. To express cell cycle stage
794 timings as progress through the unit (0-1) cell cycle, *t* was set to 1. This equation accounts
795 for the 'new cell' bias of continual replication within an asynchronous logarithmic population,
796 which results in double the number of newly divided daughter cells being present compared
797 to cells that are about to divide at the end of the previous cell cycle.

Acknowledgements

The authors would like to thank Pj Chana from Cytek Bio for useful advice, discussions and training on IFC. For the purpose of open access, the authors have applied a Creative Commons Attribution (CC BY) licence to any Author Accepted Manuscript version arising from this submission.

806 **References**

807 1. Sunter J, Gull K. Shape, form, function and Leishmania pathogenicity: from textbook
808 descriptions to biological understanding. Open Biol. 2017;7(9).
809 2. Wheeler RJ, Gluenz E, Gull K. The cell cycle of Leishmania: morphogenetic events and their
810 implications for parasite biology. Mol Microbiol. 2011;79(3):647-62.
811 3. Minocha N, Kumar D, Rajanala K, Saha S. Kinetoplast morphology and segregation pattern as
812 a marker for cell cycle progression in Leishmania donovani. J Eukaryot Microbiol. 2011;58(3):249-53.
813 4. Ambit A, Woods KL, Cull B, Coombs GH, Mottram JC. Morphological events during the cell
814 cycle of Leishmania major. Eukaryot Cell. 2011;10(11):1429-38.
815 5. Chandra U, Yadav A, Kumar D, Saha S. Cell cycle stage-specific transcriptional activation of
816 cyclins mediated by HAT2-dependent H4K10 acetylation of promoters in Leishmania donovani. PLoS
817 Pathog. 2017;13(9):e1006615.
818 6. Damasceno JD, Marques CA, Beraldi D, Crouch K, Lapsley C, Obonaga R, et al. Genome
819 duplication in Leishmania major relies on persistent subtelomeric DNA replication. eLife.
820 2020;9:e58030.
821 7. Zakharova A, Albanaz ATS, Opperdoes FR, Škodová-Sveráková I, Zagirova D, Saura A, et al.
822 Leishmania guyanensis M4147 as a new LRV1-bearing model parasite: Phosphatidate phosphatase 2-
823 like protein controls cell cycle progression and intracellular lipid content. PLOS Neglected Tropical
824 Diseases. 2022;16(6):e0010510.
825 8. Corrales RM, Vaselek S, Neish R, Berry L, Brunet CD, Crobu L, et al. The kinesin of the
826 flagellum attachment zone in Leishmania is required for cell morphogenesis, cell division and
827 virulence in the mammalian host. PLoS Pathog. 2021;17(6):e1009666.
828 9. Goda K, Filby A, Nitta N. In Flow Cytometry, Image Is Everything. Cytometry A.
829 2019;95(5):475-7.
830 10. Rees PS, H.D., Filby, A. Carpenter, A.E. Doan, M. Imaging flow cytometry. Nature Reviews
831 Methods Primers. 2022;2:86.
832 11. Hildebrand M, Davis A, Abbriano R, Pugsley HR, Traller JC, Smith SR, et al. Applications of
833 Imaging Flow Cytometry for Microalgae. Methods Mol Biol. 2016;1389:47-67.
834 12. Dunker S, Boho D, Wäldchen J, Mäder P. Combining high-throughput imaging flow cytometry
835 and deep learning for efficient species and life-cycle stage identification of phytoplankton. BMC
836 Ecology. 2018;18(1):51.
837 13. Niswander LM, McGrath KE, Kennedy JC, Palis J. Improved quantitative analysis of primary
838 bone marrow megakaryocytes utilizing imaging flow cytometry. Cytometry A. 2014;85(4):302-12.
839 14. Fertrin KY, Samsel L, van Beers EJ, Mendelsohn L, Kato GJ, McCoy JP, Jr. Sickle Cell Imaging
840 Flow Cytometry Assay (SIFCA). Methods Mol Biol. 2016;1389:279-92.
841 15. Lippeveld M, Knill C, Ladlow E, Fuller A, Michaelis LJ, Saeys Y, et al. Classification of Human
842 White Blood Cells Using Machine Learning for Stain-Free Imaging Flow Cytometry. Cytometry A.
843 2020;97(3):308-19.
844 16. Samsel L, McCoy JP, Jr. Detection and Characterization of Rare Circulating Endothelial Cells
845 by Imaging Flow Cytometry. Methods Mol Biol. 2016;1389:249-64.
846 17. Dent BM, Ogle LF, O'Donnell RL, Hayes N, Malik U, Curtin NJ, et al. High-resolution imaging
847 for the detection and characterisation of circulating tumour cells from patients with oesophageal,
848 hepatocellular, thyroid and ovarian cancers. Int J Cancer. 2016;138(1):206-16.
849 18. Muchlinska A, Smentoch J, Zaczek AJ, Bednarz-Knoll N. Detection and Characterization of
850 Circulating Tumor Cells Using Imaging Flow Cytometry-A Perspective Study. Cancers (Basel).
851 2022;14(17).
852 19. Haridas V, Ranjbar S, Vorobjev IA, Goldfeld AE, Barteneva NS. Imaging flow cytometry
853 analysis of intracellular pathogens. Methods. 2017;112:91-104.

854 20. Dekel E, Rivkin A, Heidenreich M, Nadav Y, Ofir-Birin Y, Porat Z, et al. Identification and
855 classification of the malaria parasite blood developmental stages, using imaging flow cytometry.
856 Methods. 2017;112:157-66.
857 21. Power AL, Barber DG, Groenhof SRM, Wagley S, Liu P, Parker DA, et al. The Application of
858 Imaging Flow Cytometry for Characterisation and Quantification of Bacterial Phenotypes. Front Cell
859 Infect Microbiol. 2021;11:716592.
860 22. Filby A, Perucha E, Summers H, Rees P, Chana P, Heck S, et al. An imaging flow cytometric
861 method for measuring cell division history and molecular symmetry during mitosis. Cytometry Part
862 A. 2011;79A(7):496-506.
863 23. Patterson JO, Swaffer M, Filby A. An Imaging Flow Cytometry-based approach to analyse the
864 fission yeast cell cycle in fixed cells. Methods. 2015;82:74-84.
865 24. Filby A, Day W, Purewal S, Martinez-Martin N. The Analysis of Cell Cycle, Proliferation, and
866 Asymmetric Cell Division by Imaging Flow Cytometry. Methods Mol Biol. 2016;1389:71-95.
867 25. Blasi T, Hennig H, Summers HD, Theis FJ, Cerveira J, Patterson JO, et al. Label-free cell cycle
868 analysis for high-throughput imaging flow cytometry. Nat Commun. 2016;7:10256.
869 26. Rodrigues MA, Beaton-Green LA, Wilkins RC, Fenech MF. The potential for complete
870 automated scoring of the cytokinesis block micronucleus cytome assay using imaging flow
871 cytometry. Mutat Res Genet Toxicol Environ Mutagen. 2018;836(Pt A):53-64.
872 27. Wills JW, Verma JR, Rees BJ, Harte DSG, Haxhiraj Q, Barnes CM, et al. Inter-laboratory
873 automation of the in vitro micronucleus assay using imaging flow cytometry and deep learning. Arch
874 Toxicol. 2021;95(9):3101-15.
875 28. Vorobjev IA, Bekbayev S, Temirgaliyev A, Tlegenova M, Barteneva NS. Imaging Flow
876 Cytometry of Multi-Nuclearity. Methods Mol Biol. 2023;2635:87-101.
877 29. Tatrai P, Gergely F. Centrosome function is critical during terminal erythroid differentiation.
878 EMBO J. 2022;41(14):e108739.
879 30. Wortzel I, Porat Z, Seger R, Maik-Rachline G. Applying imaging flow cytometry and
880 immunofluorescence in studying the dynamic Golgi structure in cultured cells. STAR Protoc.
881 2022;3(2):101278.
882 31. Fasler-Kan E, Baiken Y, Vorobjev IA, Barteneva NS. Analysis of Nucleocytoplasmic Protein
883 Shuttling by Imaging Flow Cytometry. Methods Mol Biol. 2016;1389:127-37.
884 32. Wiedeman J, Mensa-Wilmot K. A fixable probe for visualizing flagella and plasma
885 membranes of the African trypanosome. PloS one. 2018;13(5):e0197541-e.
886 33. Hurrell BP, Schuster S, Grün E, Coutaz M, Williams RA, Held W, et al. Rapid Sequestration of
887 Leishmania mexicana by Neutrophils Contributes to the Development of Chronic Lesion. PLOS
888 Pathogens. 2015;11(5):e1004929.
889 34. Baron N, Tupperwar N, Dahan I, Hadad U, Davidov G, Zarivach R, et al. Distinct features of
890 the Leishmania cap-binding protein LeishIF4E2 revealed by CRISPR-Cas9 mediated hemizygous
891 deletion. PLOS Neglected Tropical Diseases. 2021;15(3):e0008352.
892 35. Chiboub O, Sifaoui I, Abderrabba M, Mejri M, Fernandez JJ, Diaz-Marrero AR, et al.
893 Apoptosis-like cell death upon kinetoplastid induction by compounds isolated from the brown algae
894 Dictyota spiralis. Parasit Vectors. 2021;14(1):198.
895 36. Carnielli JBT, Dave A, Romano A, Forrester S, de Faria PR, Monti-Rocha R, et al.
896 3'Nucleotidase/nuclease is required for Leishmania infantum clinical isolate susceptibility to
897 miltefosine. EBioMedicine. 2022;86:104378.
898 37. Yanase R, Moreira-Leite F, Rea E, Wilburn L, Sadlova J, Vojtkova B, et al. Formation and
899 three-dimensional architecture of Leishmania adhesion in the sand fly vector. Elife. 2023;12.
900 38. Rabinovitch PS. DNA content histogram and cell-cycle analysis. Methods Cell Biol.
901 1994;41:263-96.
902 39. Bagwell CB, Mayo SW, Whetstone SD, Hitchcox SA, Baker DR, Herbert DJ, et al. DNA
903 histogram debris theory and compensation. Cytometry. 1991;12(2):107-18.

904 40. Fox MH. A model for the computer analysis of synchronous DNA distributions obtained by
905 flow cytometry. Cytometry. 1980;1(1):71-7.
906 41. Watson JV, Chambers SH, Smith PJ. A pragmatic approach to the analysis of DNA histograms
907 with a definable G1 peak. Cytometry. 1987;8(1):1-8.
908 42. Marques CA, Dickens NJ, Paape D, Campbell SJ, McCulloch R. Genome-wide mapping reveals
909 single-origin chromosome replication in Leishmania, a eukaryotic microbe. Genome Biol.
910 2015;16:230.
911 43. Magalhaes T, Silva DKC, Teixeira JDS, De Lima JDT, Barbosa-Filho JM, Moreira DRM, et al. A
912 Betulinic Acid Derivative, BA5, Induces G0/G1 Cell Arrest, Apoptosis Like-Death, and Morphological
913 Alterations in Leishmania sp. Front Pharmacol. 2022;13:846123.
914 44. Wheeler RJ, Gull K, Gluenz E. Detailed interrogation of trypanosome cell biology via
915 differential organelle staining and automated image analysis. BMC Biol. 2012;10:1.
916 45. Halliday C, Billington K, Wang Z, Madden R, Dean S, Sunter JD, et al. Cellular landmarks of
917 Trypanosoma brucei and Leishmania mexicana. Mol Biochem Parasitol. 2019;230:24-36.
918 46. Williams F. Dynamics of microbial populations. Patten BC, editor. New York: Academic Press;
919 1971.
920 47. Ambaru B, Gangadharan GM, Subramanya HS, Gupta CM. Profilin is involved in G1 to S
921 phase progression and mitotic spindle orientation during Leishmania donovani cell division cycle.
922 PLoS One. 2022;17(3):e0265692.
923 48. Hammarton TC, Kramer S, Tetley L, Boshart M, Mottram JC. Trypanosoma brucei Polo-like
924 kinase is essential for basal body duplication, kDNA segregation and cytokinesis. Mol Microbiol.
925 2007;65(5):1229-48.
926 49. Sadlova J, Price HP, Smith BA, Votypka J, Volf P, Smith DF. The stage-regulated HASPB and
927 SHERP proteins are essential for differentiation of the protozoan parasite Leishmania major in its
928 sand fly vector, Phlebotomus papatasi. Cell Microbiol. 2010;12(12):1765-79.
929 50. Wheeler RJ. ImageJ for Partially and Fully Automated Analysis of Trypanosome Micrographs.
930 Methods Mol Biol. 2020;2116:385-408.
931 51. Peacock L, Bailey M, Carrington M, Gibson W. Meiosis and haploid gametes in the pathogen
932 *Trypanosoma brucei*. Current Biology. 2014;24(2):181-6.
933 52. Kabani S, Waterfall M, Matthews KR. Cell-cycle synchronisation of bloodstream forms of
934 Trypanosoma brucei using Vybrant DyeCycle Violet-based sorting. Mol Biochem Parasitol.
935 2010;169(1):59-62.
936 53. Siegel TN, Kawahara T, DeGrasse JA, Janzen CJ, Horn D, Cross GAM. Acetylation of histone
937 H4K4 is cell cycle regulated and mediated by HAD in Trypanosoma brucei. Molecular Microbiology.
938 2008;67(4):762-71.
939 54. Wlodkowic D, Darzynkiewicz Z. Please do not disturb: destruction of chromatin structure by
940 supravital nucleic acid probes revealed by a novel assay of DNA-histone interaction. Cytometry A.
941 2008;73(10):877-9.
942 55. Wojcik K, Dobrucki JW. Interaction of a DNA intercalator DRAQ5, and a minor groove binder
943 SYTO17, with chromatin in live cells--influence on chromatin organization and histone-DNA
944 interactions. Cytometry A. 2008;73(6):555-62.
945 56. Varga V, Moreira-Leite F, Portman N, Gull K. Protein diversity in discrete structures at the
946 distal tip of the trypanosome flagellum. Proc Natl Acad Sci U S A. 2017;114(32):E6546-E55.
947 57. Gadella TWJ, Jr., van Weeren L, Stouthamer J, Hink MA, Wolters AHG, Giepmans BNG, et al.
948 mScarlet3: a brilliant and fast-maturing red fluorescent protein. Nat Methods. 2023;20(4):541-5.
949 58. Golub M, Guillon V, Gotthard G, Zeller D, Martinez N, Seydel T, et al. Dynamics of a family of
950 cyan fluorescent proteins probed by incoherent neutron scattering. J R Soc Interface.
951 2019;16(152):20180848.
952 59. de Oliveira BCD, Assis LHC, Shiburah ME, Paiva SC, Fontes VS, de Oliveira LS, et al.
953 Synchronization of Leishmania amazonensis Cell Cycle Using Hydroxyurea. Methods Mol Biol.
954 2022;2579:127-35.

955 60. Simpson L, Braly P. Synchronization of Leishmania tarentolae by hydroxyurea. J Protozool.
956 1970;17(4):511-7.
957 61. Hassan P, Fergusson D, Grant KM, Mottram JC. The CRK3 protein kinase is essential for cell
958 cycle progression of *Leishmania mexicana*. Mol Biochem Parasitol. 2001;113:189-98.
959 62. Hammarton TC. Who Needs a Contractile Actomyosin Ring? The Plethora of Alternative
960 Ways to Divide a Protozoan Parasite. Front Cell Infect Microbiol. 2019;9:397.
961 63. Wheeler RJ, Gull K, Sunter JD. Coordination of the Cell Cycle in Trypanosomes. Annu Rev
962 Microbiol. 2019;73:133-54.
963 64. Dandugudumula R, Fischer-Weinberger R, Zilberstein D. Morphogenesis Dynamics in
964 Leishmania Differentiation. Pathogens. 2022;11(9).
965 65. Regli IB, Passelli K, Martinez-Salazar B, Amore J, Hurrell BP, Muller AJ, et al. TLR7 Sensing by
966 Neutrophils Is Critical for the Control of Cutaneous Leishmaniasis. Cell Rep. 2020;31(10):107746.
967 66. Carlsen ED, Jie Z, Liang Y, Henard CA, Hay C, Sun J, et al. Interactions between Neutrophils
968 and Leishmania braziliensis Amastigotes Facilitate Cell Activation and Parasite Clearance. J Innate
969 Immun. 2015;7(4):354-63.
970 67. Terrazas C, Oghumu S, Varikuti S, Martinez-Saucedo D, Beverley SM, Satoskar AR.
971 Uncovering Leishmania-macrophage interplay using imaging flow cytometry. J Immunol Methods.
972 2015;423:93-8.
973 68. Abidin BM, Hammami A, Stager S, Heinonen KM. Infection-adapted emergency
974 hematopoiesis promotes visceral leishmaniasis. PLoS Pathog. 2017;13(8):e1006422.
975 69. Jha B, Reverte M, Ronet C, Prevel F, Morgenthaler FD, Desponds C, et al. In and out:
976 Leishmania metastasis by hijacking lymphatic system and migrating immune cells. Front Cell Infect
977 Microbiol. 2022;12:941860.
978 70. Miller HW, Suleiman RL, Ralston KS. Trogocytosis by Entamoeba histolytica Mediates
979 Acquisition and Display of Human Cell Membrane Proteins and Evasion of Lysis by Human Serum.
980 mBio. 2019;10(2).
981 71. Chia WN, Lee YQ, Tan KS. Imaging flow cytometry for the screening of compounds that
982 disrupt the Plasmodium falciparum digestive vacuole. Methods. 2017;112:211-20.
983 72. Beneke T, Madden R, Makin L, Valli J, Sunter J, Gluenz E. A CRISPR Cas9 high-throughput
984 genome editing toolkit for kinetoplastids. R Soc Open Sci. 2017;4(5):170095.
985 73. Beneke T, Gluenz E. LeishGEdit: A Method for Rapid Gene Knockout and Tagging Using
986 CRISPR-Cas9. In: Clos J, editor. Leishmania: Methods and Protocols. New York, NY: Springer New
987 York; 2019. p. 189-210.
988 74. Schneider CA, Rasband WS, Eliceiri KW. NIH Image to ImageJ: 25 years of image analysis. Nat
989 Methods. 2012;9(7):671-5.
990 75. IDEAS User Manual v6 [Available from:
991 https://www.pedsresearch.org/uploads/pages/img/IDEAS_User_Manual_6.pdf.

992

993

994

995

996 **Supporting information captions**

997 **S1 Fig. Cell cycle-dependent morphologies of *L. mexicana*.** A representation of the
998 morphological changes seen as a cell progresses through the different cell cycle stages. The
999 relative timings of the cell cycle stages are not to scale. M: mitosis; C: cytokinesis; N:
1000 nucleus; K: kinetoplast; F: flagellum.

1001 **S2 Fig. Intensity profiles of *L. mexicana* promastigote cells stained with various DNA**
1002 **dyes.** C9T7 cells were incubated with the various dyes, as detailed in the Materials and
1003 Methods, before being analysed on the ImageStream. Each intensity profile shows the data
1004 acquired from ~30,000 cells, with example images below (left panel: brightfield image; right
1005 panel: fluorescence image; scale bars 7 µm). (A) Methanol-fixed cells stained with propidium
1006 iodide. (B) Cell cycle modelling of the propidium iodide DNA intensity profile (panel A) using
1007 the FCS Express™ Multicycle engine (Rabinovitch & Bagwell debris subtraction (38, 39) and
1008 Dean/Jett/Fox cell cycle modelling (40)). The cell cycle stages of each curve are indicated.
1009 C-F: live cells stained with Hoechst, DRAQ5, Vybrant™ DyeCycle™ Violet and Vybrant™
1010 DyeCycle™ Ruby, respectively.

1011 **S3 Fig. DCO does not affect viability of *L. mexicana* promastigotes.** Following
1012 incubation with DCO, C9T7 cells were washed three times in PBS and resuspended in M199
1013 at a density of 5 x 10^5 cellsml^{-1}. Control (unstained) cells were similarly processed. Cell
1014 density was measured over 72 hours and a growth curve plotted.

1015 **S4 Fig. Stability of DCO.** (A) Triplicate populations of *L. mexicana* promastigote C9T7 cells
1016 were stained with 0.625 µM DCO for 30 minutes at room temperature before being
1017 resuspended in PBS. Following resuspension in PBS, cell samples were analysed by IFC at
1018 the time points indicated. Fluorescence intensity profiles are shown for one representative
1019 replicate (n = ~15,000 cells).

1020 **S5 Fig. Morphological parameters of different cell cycle stages.** *L. mexicana* C9T7
1021 promastigotes were stained with DCO, analysed by IFC and gated according to their DNA

1022 intensity (2C, intermediate DNA content (Int.; 2C-4C) and 4C) (Fig. 3A). The area, aspect
1023 ratio (AR), brightfield intensity (BF_Intensity), circularity, compactness, diameter,
1024 elongatedness, height, perimeter, shape ratio and thickness_min of the cells were then
1025 plotted for each gate, as indicated in the figure.

1026 **S6 Fig. Linking DNA content and cellular dimensions.** (A) Length and (B) width
1027 distributions of C9T7 cells from the DNA intensity plot presented in Fig 3A. Top panels: cells
1028 within the 2C gate; middle panels: cells within the intermediate (2C-4C) gate; bottom: overlay
1029 of cells in all gates.

1030 **S7 Fig. Morphological parameters of cells gated on DNA content and length.** *L.*
1031 *mexicana* C9T7 promastigotes were stained with DCO, analysed by IFC and gated
1032 according to their DNA intensity (2C, intermediate DNA content (Int.; 2C-4C) and 4C) (Fig.
1033 3A). 4C gated cells were then further gated according to their length (short: <10 μm; long ≥
1034 10 μm) (Fig 3B). The area, aspect ratio (AR), brightfield intensity (BF_Intensity), circularity,
1035 compactness, diameter, elongatedness, height, length, perimeter, shape ratio,
1036 thickness_min and width of the cells in each gate were then plotted, as indicated in the
1037 figure.

1038 **S8 Fig. S phase cells with elongated mNG:KINF fluorescence.** Some long, narrow C9T7
1039 mNG:KINF cells with a single flagellum were observed to possess a single elongated focus
1040 of mNG:KINF fluorescence that led to them being classified automatically as having a mitotic
1041 spindle. Cells such as these were manually removed from the 'mNG:KINF spindle'
1042 population and added to the S phase 1CF population.

1043 **S9 Fig. Dimensions of G2 phase cells.** The lengths (A) and widths (B) of C9T7 mNG:KINF
1044 cells identified as being in G2 phase were plotted.

1045 **S10 Fig. Fluorescence intensity plot of C9T7 mNG:KINF cells stained with DCO.** Cells
1046 were imaged with a laser power of 3 mW to excite only DCO and not mNG:KINF to
1047 detectable levels. 2C, intermediate (2C-4C) and 4C gates were placed as indicated (blue

1048 boxes) with the % cells within each of the gates indicated on the right. Data was from the
1049 Run 2 replicate; data from the Runs 1 and 3 replicates is in S1G Table.

1050 **S11 Fig. ImageStream cell gating strategy.** Following ImageStream acquisition, data were
1051 processed using a user-defined gating strategy in IDEAS to identify single cells and gate out
1052 doublets, debris and images with artefacts. First, cell body area was plotted against side
1053 scatter, with gating applied to exclude debris and speed beads (A; teal gate). Next, singlet
1054 cells were selected using a cell body area vs aspect ratio plot (B; blue gate). The best in
1055 focus cells in bright field (BIF_BF) were identified via the Gradient_RMS parameter (C;
1056 orange bar). Images with a single mask (i.e. one object per image) were selected using
1057 "Spot Count" (D) and plotting cell body area against cell compactness enabled the removal
1058 of overlapping cells, resulting in the 'Processed' population (E, light blue gate), which was
1059 then utilised for morphological and fluorescence analysis. *n* = 30,000 C9T7 cells.

1060 **S12 Fig. ImageStream cell cycle gating strategy.** Using a 'processed' population (Fig.
1061 S11), separate gating strategies were employed for the cell cycle analysis of DCO-stained
1062 C9T7 mNG:KINF cells excited with a laser power of 3 mW (A) and unstained C9T7
1063 mNG:KINF cells excited with a laser power of 120 mW (B). (A) The best in-focus DNA
1064 images were selected using Gradient_RMS (I; red bar) and cells sufficiently stained with
1065 DCO were identified via their fluorescent intensity (ii; orange gate). The cell cycle stages of
1066 the cells were then determined based on their DCO intensity (iii; G1, S and G2/M bars). To
1067 facilitate further resolution of cell cycle stage within the G2/M cell population, morphological
1068 characteristics were analysed. Cell body length (iv) and width (v; using the Thickness Max
1069 parameter) were plotted to identify short (length ≤10 μm), long (length >10 μm), narrow
1070 (width ≤4 μm) and wide (width >4 μm) cells. (B) Cells expressing mNG:KINF were identified
1071 by gating on green fluorescence greater than that of the parental untagged cell line (i; green
1072 gate). Cell cycle stages were determined from the cell length (ii, short and long bars, as in
1073 (A)) and width (iii; Thickness Max, narrow and wide bars, as in (A)) and by their mNG:KINF
1074 fluorescence pattern. mNG:KINF foci were identified using masks, allowing the separation of

1075 cells with one or two mNG:KINF foci (iv). The aspect ratio intensity of cells with a single
1076 mNG:KINF focus allowed cells with a circular focus or an elongated spindle-shaped focus to
1077 be distinguished (v).

1078 **S13 Fig. Aberrant mNG:KINF populations.** Example images of C9T7 mNG:KINF cells that
1079 were discarded from further analysis. (A) short, wide cells with mNG fluorescence below the
1080 threshold. The majority of these cells had aberrant morphology that meant they could not be
1081 assigned to any given cell cycle stage. (B) cells assigned by IDEAS™ as long and wide with
1082 two circular mNG:KINF foci. The majority of images from this group were found to be of two
1083 individual cells in close proximity that had been misclassified. (C) short narrow cells that
1084 were classified as having two circular mNG:KINF foci by IDEAS™. All of these cells were
1085 found to have unequally sized foci, suggesting that there was some additional fluorescence
1086 in the region of the kinetoplast (white arrowheads).

1087 **S1 Table. Raw and compiled IFC data.** (A) Live vs fixed raw data. Length and width
1088 measurements used to compile Fig 1D. (B) DCO vs PI percentages. Cell cycle modelling
1089 data from triplicate IFC analysis of C9T7 cells stained with DCO or PI as used to compile Fig
1090 2D. (C-E) KINF Run1-3. Raw and processed data from triplicate IFC analysis of unstained
1091 mNG:KINF cells analysed with a laser power of 120 mW. Further details are given in the
1092 'Notes' section at the bottom of the worksheet. (F) KINF averages. Mean values + standard
1093 deviations for data from the three mNG:KINF replicates, used to compile Fig 5B,D. (G) DCO.
1094 Gate data from triplicate IFC analysis of DCO-stained mNG:KINF cells analysed with a laser
1095 power of 3 mW. Run 2 data is presented in S10 Fig. (H) Calculated timings. Compiled
1096 mNG:KINF and DCO IFC data used to generate the cell cycle stage durations presented in
1097 Table 1 and Fig 7. Further details are given in the 'Notes' section at the bottom of the
1098 worksheet.

1099

1100